



ATLAS Note

GROUP-2017-XX

23rd January 2021



1

2 WZ + Heavy Flavor Production in pp collisions 3 at $\sqrt{s} = 13$ TeV

4

The ATLAS Collaboration

5

A measurement of WZ produced with an associated heavy flavor jet is performed using 140
6 fb^{-1} of proton-proton collision data at $\sqrt{s} = 13$ TeV from the ATLAS experiment at the
7 LHC. The measurement is performed in the fully leptonic decay mode, $\text{WZ} \rightarrow \ell\bar{\nu}\ell\bar{\nu}$. The
8 cross-section of $\text{WZ} + b\text{-jets}$ is measured to be $X \pm X \pm X$, while the cross-section of $\text{WZ} +$
9 charm is measured as X , with a correlation of X between the two processes.

10

© 2021 CERN for the benefit of the ATLAS Collaboration.

Reproduction of this article or parts of it is allowed as specified in the CC-BY-4.0 license.

11 **Contents**

12	1 Changes and outstanding items	3
13	1.1 Changelog	3
14	1.1.1 Changes relative to v3	3
15	1.1.2 Changes relative to v2	4
16	1.1.3 Changes relative to v1	4
17	1.2 Outstanding Items	4
18	2 Executive Summary	5
19	3 Data and Monte Carlo Samples	5
20	3.1 Data Samples	6
21	3.2 Monte Carlo Samples	6
22	4 Object Reconstruction	7
23	4.1 Trigger	7
24	4.2 Light leptons	7
25	4.3 Jets	8
26	4.4 B-tagged Jets	10
27	4.5 Missing transverse energy	11
28	5 Event Selection and Signal Region Definitions	11
29	5.1 Event Preselection	11
30	5.2 Fit Regions	14
31	5.3 Non-Prompt Lepton Estimation	29
32	5.3.1 $t\bar{t}$ Validation	29
33	5.3.2 Z+jets Validation	33
34	6 tZ Interference Studies and Separation Multivariate Analysis	37
35	6.1 Interference Studies	38
36	6.2 Top Mass Reconstruction	39
37	6.3 tZ BDT	40
38	7 Systematic Uncertainties	43
39	8 Results	46
40	8.1 1-jet Fit Results	47
41	8.2 2-jet Fit Results	53
42	9 Conclusion	57

43 **1 Changes and outstanding items**

44 **1.1 Changelog**

45 This is version 4

46 **1.1.1 Changes relative to v3**

- 47 • Merged introduction into executive summary, including unblinding details and list of
48 SRs/CRs used
- 49 • listed ptag used (p4133), and release (AB 21.2.127)
- 50 • Included table reftab:xsecUnc listing x-sec uncertainties used
- 51 • Removed selection criteria listed in table 4 (QMisID, AmbiguityType) that were removed
52 from the analysis
- 53 • specified variable used to make truth jet flavor determination (HadronConeExclTruthLa-
54 belIID)
- 55 • fixed bug in MtLepMet calculation, updated selection/fits to account for this
- 56 • Included plots of MtLepMet and PtZ, swapped lep 1 and 2 p_T plots for lep W and lep Z
57 plots
- 58 • updated tZ BDT training to reduce overfitting, updated plots to include error bars, feature
59 importance
- 60 • updated table 8 to clarify selection, fix the tZ_BDT cut used
- 61 • replace a few broken ntuples which included large weight events
- 62 • include DL1r distribution for Z+jets and $t\bar{t}$ VRs
- 63 • Expanded section on fakes, included information on derived scale factors from VRs.
- 64 • Changed the kinematic plots to include $p_T(Z)$ and $m_T(W)$, list lepton p_T based on W and
65 Z candidates.

66 **1.1.2 Changes relative to v2**

- 67 • Added alternate VBS samples to include missing b-jet diagrams
68 • Included a section on tZ interference effects, [6.1](#).
69 • Updated to reflect changes for 2018, including the move to PFlow jets, DL1r, updated
70 trigger, and updated AnalysisBase version (now 21.2.127)
71 • Revised fit regions, using separate 1-jet and 2-jet fits, with all 2-j regions included
72 • updated plots for tZ BDT, added details about the model
73 • Included truth jet information

74 **1.1.3 Changes relative to v1**

- 75 • Added GRL list
76 • Fixed latex issue in line 92, typo in line 172
77 • Added tables [6](#) and [4](#), summarizing the event and object selection
78 • Added table [2](#), which includes the DSID of samples used
79 • Included reference to WZ inclusive paper in introduction

80 **1.2 Outstanding Items**

- 81 • Unblind, update plots and fits to include data
82 • Include truth jet studies
83 • Add cross-section, significance once unblinded

84 2 Executive Summary

85 The production of WZ in association with a heavy flavor jet represents an important background
 86 for many major analyses. This includes any process with leptons and b-jets in the final state,
 87 such as $t\bar{t}H$, $t\bar{t}W$, and $t\bar{t}Z$. While precise measurements have been made of WZ production
 88 [1], $WZ +$ heavy flavor remains poorly understood. This is largely because the QCD processes
 89 involved in the production of the b-jet make it difficult to simulate accurately. This introduces a
 90 large uncertainty for analyses that include this process as a background.

91 Motivated by its relevance to the $t\bar{t}H$ multilepton analysis, we perform a study of the fully
 92 leptonic decay mode of this channel; that is, events where both the W and Z decay leptonically.
 93 Because WZ has no associated jets at leading order, while the major backgrounds for this channel
 94 tend to have high jet multiplicity, events with more than two jets are rejected. This gives a final
 95 state signature of three leptons and one or two jets.

96 Events that meet this selection criteria are sorted into pseudo-continuous b-tagging regions based
 97 on the DL1r b-tag score of their associated jets. This is done to separate $WZ +$ b-jet events
 98 from $WZ +$ charm and $WZ +$ light jets. These orthogonal categories, in addition to a tZ Control
 99 Region formed using an MVA, are the Signal Regions for the analysis. These regions are fit to
 100 data in order make a more accurate estimate of the contribution of $WZ +$ heavy-flavor, where
 101 heavy-flavor jets include b-jets and charm jets. Separate fits are performed for 1-jet and 2-jet
 102 events. The full Run-2 dataset collected by the ATLAS detector, representing 139 fb^{-1} of data
 103 from pp collisions at $\sqrt{s} = 13 \text{ TeV}$, is used for this study.

104 All backgrounds are accounted for using Monte Carlo, with the simulation of non-prompt lepton
 105 backgrounds - $Z+jets$ and $t\bar{t}$ - validated using non-prompt Validation Regions.

106 Section 3 details the data and Monte Carlo (MC) samples used in the analysis. The reconstruction
 107 of various physics objects is described in section 4. Section 5 describes the event selection applied
 108 to these samples, along the definitions of the various regions used in the fit. The multivariate
 109 analysis techniques used to separate the tZ background from $WZ +$ heavy flavor are described in
 110 section 6. Section 7 describes the various sources of systematic uncertainties considered in the
 111 fit. Finally, the results of the analysis are summarized in section 8, followed by a brief conclusion
 112 in section 9.

113 The current state of the analysis shows blinded results for the full 2018 dataset. Regions containing
 114 $>5\%$ $WZ+b$ events are blinded, and results are from Asimov, MC only fits. In addition to adding
 115 some additional information to this note, remaining tasks include performing WZ/tZ interference
 116 studies, finalizing the presentation of results, and unblinding.

117 3 Data and Monte Carlo Samples

118 Both data and Monte Carlo samples used in this analysis were prepared in the xAOD format,
 119 which was used to produce a Dx AOD sample in the HIGG8D1 derivation framework. The HIGG8D1

120 framework is designed for the $t\bar{t}H$ multi-lepton analysis, which targets events with multiple
 121 leptons as well as tau hadrons. This framework skims the dataset to remove unneeded variables
 122 as well as entire events. Events are removed from the derivations that do not meet the following
 123 selection:

- 124 • at least two light leptons within a range $|\eta| < 2.6$, with leading lepton $p_T > 15$ GeV and
 125 subleading lepton $p_T > 5$ GeV
- 126 • at least one light lepton with $p_T > 15$ GeV within a range $|\eta| < 2.6$, and at least two hadronic
 127 taus with $p_T > 15$ GeV.

128 Samples were then generated from these HIGG8D1 derivations with p-tag of p4134 using a
 129 modified version of AnalysisBase version 21.2.127.

130 3.1 Data Samples

131 The study uses a sample of proton-proton collision data collected by the ATLAS detector from
 132 2015 through 2018 at an energy of $\sqrt{s} = 13$ TeV, which represents an integrated luminosity of
 133 139 fb^{-1} . This data set was collected with a bunch crossing rate of 25 ns. All data used in this
 134 analysis was verified by data quality checks, having been included in the following Good Run
 135 Lists:

- 136 • data15_13TeV.periodAllYear_DetStatus-v79-repro20-02_DQDefects-00-02-02
 137 _PHYS_StandardGRL_All_Good_25ns.xml
- 138 • data16_13TeV.periodAllYear_DetStatus-v88-pro20-21_DQDefects-00-02-04
 139 _PHYS_StandardGRL_All_Good_25ns.xml
- 140 • data17_13TeV.periodAllYear_DetStatus-v97-pro21-13_Unknown_PHYS_StandardGRL
 141 _All_Good_25ns_Triggerno17e33prim.xml
- 142 • data18_13TeV.periodAllYear_DetStatus-v102-pro22-04_Unknown_PHYS_StandardGRL
 143 _All_Good_25ns_Triggerno17e33prim.xml

144 Runs included from the AllYear period containers are included.

145 3.2 Monte Carlo Samples

146 Several different generators were used to produce Monte Carlo simulations of the signal and
 147 background processes. For all samples, the response of the ATLAS detector is simulated using
 148 Geant4. The WZ signal samples are simulated using Sherpa 2.2.2 [2]. Specific information
 149 about the Monte Carlo samples being used can be found in table 1. A list of the specific samples
 150 used by data set ID is shown in table 2.

Table 1: The configurations used for event generation of signal and background processes, including the event generator, matrix element (ME) order, parton shower algorithm, and parton distribution function (PDF).

Process	Event generator	ME order	Parton Shower	PDF
WZ, VV	SHERPA 2.2.2	MEPS NLO	SHERPA	CT10
tZ	MG5_AMC	LO	PYTHIA 6	CTEQ6L1
t̄W	MG5_AMC (SHERPA 2.1.1)	NLO (LO multileg)	PYTHIA 8 (SHERPA)	NNPDF 3.0 NLO (NNPDF 3.0 NLO)
t̄(Z/γ* → ll)	MG5_AMC	NLO	PYTHIA 8	NNPDF 3.0 NLO
t̄H	MG5_AMC (MG5_AMC)	NLO (NLO)	PYTHIA 8 (HERWIG++)	NNPDF 3.0 NLO [Ball:2014uwa] (CT10 [ct10])
tHqb	MG5_AMC	LO	PYTHIA 8	CT10
tHW	MG5_AMC (SHERPA 2.1.1)	NLO (LO multileg)	HERWIG++ (SHERPA)	CT10 (NNPDF 3.0 NLO)
tWZ	MG5_AMC	NLO	PYTHIA 8	NNPDF 2.3 LO
t̄t, t̄t̄t̄	MG5_AMC	LO	PYTHIA 8	NNPDF 2.3 LO
t̄W+W-	MG5_AMC	LO	PYTHIA 8	NNPDF 2.3 LO
t̄t	Powheg-BOX v2 [powheggtt]	NLO	PYTHIA 8	NNPDF 3.0 NLO
t̄t̄γ	MG5_AMC	LO	PYTHIA 8	NNPDF 2.3 LO
s-, t-channel, Wt single top	Powheg-BOX v1 [powhegstp]	NLO	PYTHIA 6	CT10
qqVV, VVV Z → l+l-	SHERPA 2.2.1	MEPS NLO	SHERPA	NNPDF 3.0 NLO

4 Object Reconstruction

All regions defined in this analysis share a common lepton, jet, and overall event preselection. The selection applied to each physics object is detailed here; the event preselection, and the selection used to define the various fit regions, is described in section 5.

4.1 Trigger

Events are required to be selected by dilepton triggers, as summarized in table 3.

4.2 Light leptons

Electron candidates are reconstructed from energy clusters in the electromagnetic calorimeter that are associated with charged particle tracks reconstructed in the inner detector [3]. Electron candidates are required to have $p_T > 10$ GeV and $|\eta_{\text{cluster}}| < 2.47$. Candidates in the transition region between different electromagnetic calorimeter components, $1.37 < |\eta_{\text{cluster}}| < 1.52$, are rejected. A multivariate likelihood discriminant combining shower shape and track information is used to distinguish real electrons from hadronic showers (fake electrons). To further reduce

Sample	DSID
WZ	364253, 364739-42
VV	364250, 364254, 364255, 363355-60, 364890
t̄W	410155
t̄Z	410156, 410157, 410218-20
low mass t̄Z	410276-8
Rare Top	410397, 410398, 410399
single Top	410658-9, 410644-5
three Top	304014
four Top	410080
t̄WW	410081
Z + jets	364100-41
low mass Z + jets	364198-215
W + jets	364156-97
Vγ	364500-35
tZ	410560
tW	410013-4
WtZ	410408
VVV	364242-9
VH	342284-5
WtH	341998
t̄tγ	410389
t̄t	410470
t̄tH	345873-5, 346343-5

Table 2: List of Monte Carlo samples by data set ID used in the analysis.

164 the non-prompt electron contribution, the track is required to be consistent with originating from
 165 the primary vertex; requirements are imposed on the transverse impact parameter significance
 166 ($|d_0|/\sigma_{d_0}$) and the longitudinal impact parameter ($|\Delta z_0 \sin \theta_\ell|$), as shown in table 4.

167 Muon candidates are reconstructed by combining inner detector tracks with track segments or
 168 full tracks in the muon spectrometer [4]. Muon candidates are required to have $p_T > 10$ GeV
 169 and $|\eta| < 2.5$.

170 All leptons are required to be isolated, and pass a non-prompt BDT selection described in detail
 171 in [5].

172 4.3 Jets

173 Jets are reconstructed from calibrated topological clusters built from energy deposits in the
 174 calorimeters [6], using the anti- k_t algorithm with a radius parameter $R = 0.4$. Jets with energy
 175 contributions likely arising from noise or detector effects are removed from consideration [7],

Dilepton triggers (2015)		
$\mu\mu$ (asymm.)	HLT_mu18_mu8noL1	
ee (symm.)	HLT_2e12_lhloose_L12EM10VH	
$e\mu, \mu e$ (\sim symm.)	HLT_e17_lhloose_mu14	
Dilepton triggers (2016)		
$\mu\mu$ (asymm.)	HLT_mu22_mu8noL1	
ee (symm.)	HLT_2e17_lhvloose_nod0	
$e\mu, \mu e$ (\sim symm.)	HLT_e17_lhloose_nod0_mu14	
Dilepton triggers (2017)		
$\mu\mu$ (asymm.)	HLT_mu22_mu8noL1	
ee (symm.)	HLT_2e24_lhvloose_nod0	
$e\mu, \mu e$ (\sim symm.)	HLT_e17_lhloose_nod0_mu14	
Dilepton triggers (2018)		
$\mu\mu$ (asymm.)	HLT_mu22_mu8noL1	
ee (symm.)	HLT_2e24_lhvloose_nod0	
$e\mu, \mu e$ (\sim symm.)	HLT_e17_lhloose_nod0_mu14	

Table 3: List of lowest p_T -threshold, un-prescaled dilepton triggers used for 2015-2018 data taking.

	e			μ						
	L	L^*	T	L	L^*	T				
FixedCutLoose	No	Yes		No	Yes					
Non-prompt lepton BDT	No	Yes		No	Yes					
Identification	Loose	Tight		Loose	Medium					
Transverse impact parameter significance $ d_0 /\sigma_{d_0}$	< 5			< 3						
Longitudinal impact parameter $ z_0 \sin \theta $	< 0.5 mm									

Table 4: Loose (L), loose and minimally-isolated (L^*), and tight (T) light lepton definitions.

and only jets satisfying $p_T > 25$ GeV and $|\eta| < 2.5$ are used in this analysis. For jets with $p_T < 60$ GeV and $|\eta| < 2.4$, a jet-track association algorithm is used to confirm that the jet originates from the selected primary vertex, in order to reject jets arising from pileup collisions [8].

180 **4.4 B-tagged Jets**

181 In order to make a measurement of $WZ +$ heavy flavor it is necessary to distinguish these events
 182 from $WZ +$ light jets. For this purpose, the DL1r b-tagging algorithm is used to distinguish
 183 heavy flavor jets from lighter ones. The DL1r algorithm uses jet kinematics, particularly jet
 184 vertex information, as input for a neural network which assigns each jet a score designed to
 185 reflect how likely that jet is to have originated from a b-quark.

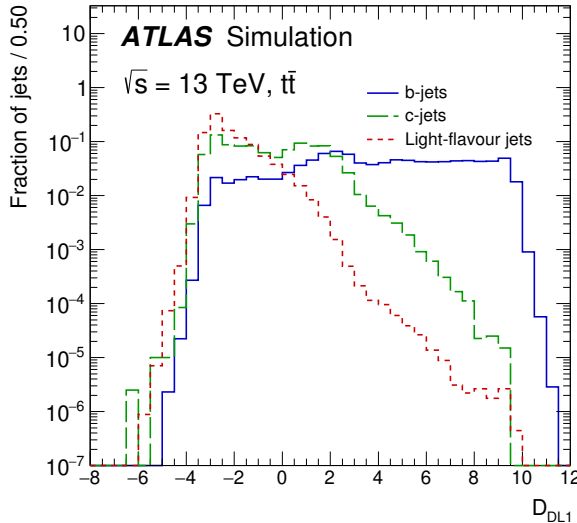


Figure 1: Output distribution of the DL1r algorithm for b-jets, charm jets, and light jets

186 From the output of the BDT, working points (WPs) are developed based on the efficiency of truth
 187 b-jets at particular values of the DL1r algorithm. The working points used in this analysis are
 188 summarized in table 5.

WP	none	loose	medium	tight	tightest
b eff.	-	85%	77%	70%	60%

Table 5: B-tagging Working Points by tightness and b-jet efficiency

189 A tighter WP will accept fewer b-jets, but reject a higher fraction of charm and light jets.
 190 Generally, analyses that include b-jets will use a fixed working point, for example, requiring that
 191 a jet pass the 70% threshold. By instead treating these working point as bins, e.g. events with
 192 jets that fall between the 85% and 77% WPs fall into one bin, while events with jets passing the
 193 60% WP fall into another, and looking at the full psuedo-continuous DL1r spectrum of the jets,
 194 additional information can be gained. The psuedo-continuous b-tag spectrum is used in this case
 195 to separate out $WZ + b$, $WZ + \text{charm}$, and $WZ + \text{light}$.

¹⁹⁶ **4.5 Missing transverse energy**

¹⁹⁷ Missing transverse momentum (E_T^{miss}) is used as part of the event selection. The missing
¹⁹⁸ transverse momentum vector is defined as the inverse of the sum of the transverse momenta of
¹⁹⁹ all reconstructed physics objects as well as remaining unclustered energy, the latter of which is
²⁰⁰ estimated from low- p_T tracks associated with the primary vertex but not assigned to a hard object,
²⁰¹ with object definitions taken from [9]. Light leptons considered in the E_T^{miss} reconstruction are
²⁰² required to have $p_T > 10$ GeV, while jets are required to have $p_T > 20$ GeV.

²⁰³ **5 Event Selection and Signal Region Definitions**

²⁰⁴ Events are required to pass a preselection described in section 5.1 and summarized in table 6.
²⁰⁵ Those that pass this preselection are divided into various fit regions described in section 5.2,
²⁰⁶ based on the number of jets in the event, and the b-tag score of those jets.

²⁰⁷ **5.1 Event Preselection**

²⁰⁸ Events are required to include exactly three reconstructed light leptons passing the requirement
²⁰⁹ described in 4.2, which have a total charge of ± 1 . As the opposite sign lepton is found to
²¹⁰ be prompt the vast majority of the time [5], it is required to be loose and isolated, as defined
²¹¹ through the standard `isolationFixedCutLoose` working point supported by combined per-
²¹² formance groups. The same sign leptons are required to be very tight, as per the recommended
²¹³ `isolationFixedCutTight`.

²¹⁴ The leptons are ordered in the analysis code as 0, 1, and 2. Lepton 0 is the lepton whose charge
²¹⁵ is opposite the other two. Lepton 1 is the lepton closest to the opposite charge lepton, i.e. the
²¹⁶ smallest ΔR , leaving lepton 2 as the lepton further from the opposite charge lepton. Lepton 0
²¹⁷ is required to have $p_T > 10$ GeV, while the same sign leptons, 1 and 2, are required to have
²¹⁸ $p_T > 20$ GeV to reduce the contribution of non-prompt leptons.

²¹⁹ The invariant mass of at least one pair of opposite sign, same flavor leptons is required to fall
²²⁰ within 10 GeV of the mass of the Z boson, 91.2 GeV. Events where one of the opposite sign pairs
²²¹ have an invariant mass less than 12 GeV are rejected in order to suppress low mass resonances.

²²² An additional requirement is placed on the missing transverse energy, $E_T^{\text{miss}} > 20$ GeV, and the
²²³ transverse mass of the W candidate, $m(E_T^{\text{miss}} + l_{\text{other}}) > 30$ GeV, where E_T^{miss} is the missing
²²⁴ transverse energy, and l_{other} is the lepton not included in the Z-candidate.

²²⁵ Events are required to have one or two reconstructed jets passing the selection described in
²²⁶ section 4.3. Events with more than two jets are rejected in order to reduce the contribution of
²²⁷ backgrounds such as $t\bar{t}Z$ and $t\bar{t}W$, which tend to have higher jet multiplicity.

Event Selection
Exactly three leptons with charge ± 1
Two same-charge leptons with $p_T > 20 \text{ GeV}$
One opposite charge lepton with $p_T > 10 \text{ GeV}$
$m(l^+l^-)$ within 10 GeV of 91.2 GeV
Transverse mass of W-candidate, $m_T(E_T^{\text{miss}} + \text{lep}_{\text{other}}) > 30 \text{ GeV}$
Missing transverse energy, $E_T^{\text{miss}} > 20 \text{ GeV}$
One or two jets with $p_T > 25 \text{ GeV}$

Table 6: Summary of the selection applied to events for inclusion in the fit

228 The event yields in the preselection region for both data and Monte Carlo are summarized in
 229 table 5.1, which shows good agreement between data and Monte Carlo, and demonstrates that
 230 this region consists primarily of WZ events. The WZ events are split into WZ + b, WZ + c, and
 231 WZ + 1 based on the truth flavor of the heaviest associated jet in the event. Specifically, this
 232 determination is made based on the HadronConeExclTruthLabelID of the jet. That is, WZ +
 233 1 events contain no charm and b jets at truth level, WZ + c contain at least one truth charm and
 234 no b-jets, and WZ + b contains at least one truth b-jet.

Process	Events
$WZ + b$	167.64 ± 6.45
$WZ + c$	1080.91 ± 39.28
$WZ + l$	7223.37 ± 312.53
Other VV	849.79 ± 142.13
$t\bar{t}W$	16.81 ± 2.31
$t\bar{t}Z$	114.68 ± 17.40
rare Top	2.20 ± 0.14
Single top	0.10 ± 0.45
Three top	0.01 ± 0.01
Four top	0.02 ± 0.01
$t\bar{t}WW$	0.23 ± 0.05
$Z + \text{jets}$	601.16 ± 260.13
$V + \gamma$	36.51 ± 54.34
tZ	194.64 ± 65.74
tW	5.49 ± 1.24
WtZ	25.80 ± 1.07
VVV	26.21 ± 0.87
VH	94.34 ± 7.35
$t\bar{t}$	107.68 ± 8.14
$t\bar{t}H$	4.28 ± 0.46
Total	10556.8 ± 533.4
Data	10574

Table 7: Events yields in the preselection region at 138.9 fb^{-1}

²³⁵ Here Other VV represents diboson processes other than WZ, and consists predominantly of
²³⁶ $ZZ \rightarrow ll\bar{l}\bar{l}$ events where one of the leptons is not reconstructed.

²³⁷ Simulations are further validated by comparing the kinematic distributions of the Monte Carlo
²³⁸ with data, which are shown in figures 2. Here, bins with 5% or more WZ+b are blinded.

WZ Fit Region - Inclusive

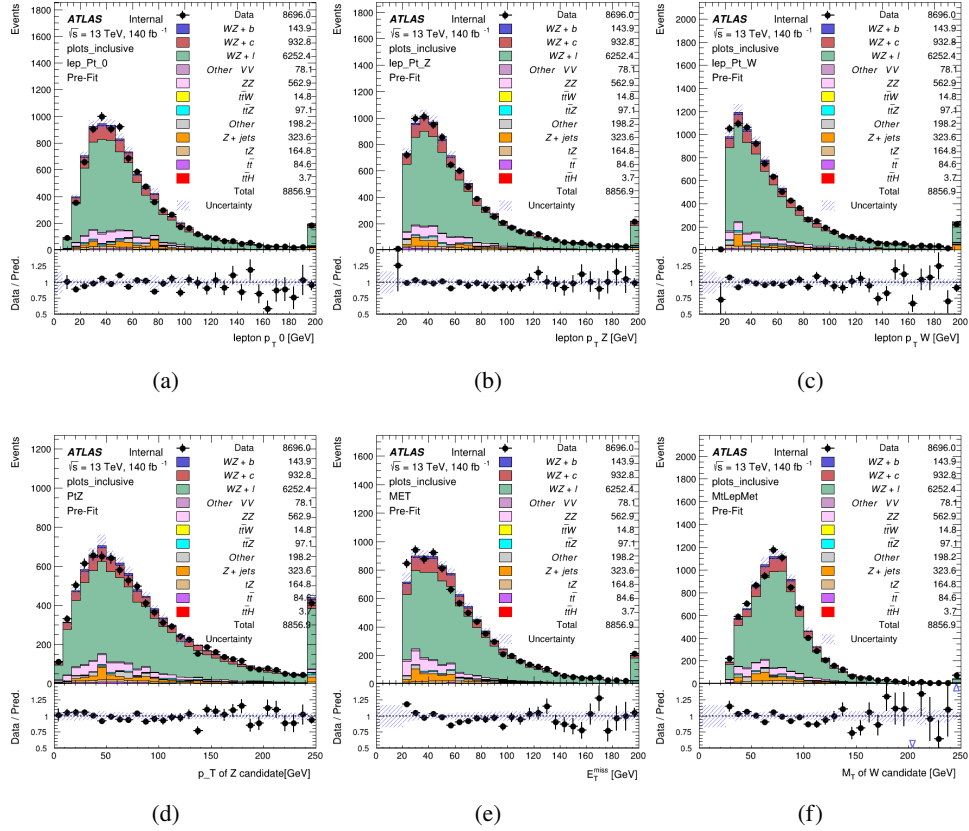


Figure 2: Comparisons between the data and MC distributions in the preselection region for (a) the p_T of the opposite sign lepton, (b) the p_T of the other lepton from the Z candidate, (c) the p_T of the lepton from the W candidate, (d) the p_T of the Z candidate, (e) the E_T^{miss} , and (f) the m_T of the W candidate.

5.2 Fit Regions

Once preselection has been applied, the remaining events are categorized into one of twelve orthogonal regions. The regions used in the fit are summarized in table 8.

The working points discussed in section 4.4 are used to separate events into fit regions based on the highest working point reached by a jet in each event. Because the background composition differs significantly based on the number of b-jets, events are further subdivided into 1 jet and 2 jet regions in order to minimize the impact of background uncertainties.

An additional tZ control region is created based on the BDT described in section 6. The region with 1-jet passing the 60% working point is split in two - a signal enriched region of events with a BDT score greater than 0.03, and a tZ control region including events with less than 0.03. This

Table 8: A list of the regions used in the fit and the selection used for each.

Region	Selection
1j, <85%	$N_{\text{jets}} = 1, n\text{Jets_DL1r_85} = 0$
1j, 85%-77%	$N_{\text{jets}} = 1, n\text{Jets_DL1r_85} = 1, n\text{Jets_DL1r_77}=0$
1j, 77%-70%	$N_{\text{jets}} = 1, n\text{Jets_DL1r_77} = 1, n\text{Jets_DL1r_70}=0$
1j, 70%-60%	$N_{\text{jets}} = 1, n\text{Jets_DL1r_70} = 1, n\text{Jets_DL1r_60}=0$
1j, >60%	$N_{\text{jets}} = 1, n\text{Jets_DL1r_60} = 1, tZ \text{ BDT} > 0.725$
1j tZ CR	$N_{\text{jets}} = 1, n\text{Jets_DL1r_60} = 1, tZ \text{ BDT} < 0.725$
2j, <85%	$N_{\text{jets}} = 2, n\text{Jets_DL1r_85} = 0$
2j, 85%-77%	$N_{\text{jets}} = 2, n\text{Jets_DL1r_85} >= 1, n\text{Jets_DL1r_77}=0$
2j, 77%-70%	$N_{\text{jets}} = 2, n\text{Jets_DL1r_77} >= 1, n\text{Jets_DL1r_70}=0$
2j, 70%-60%	$N_{\text{jets}} = 2, n\text{Jets_DL1r_70} >= 1, n\text{Jets_DL1r_60}=0$
2j, >60%	$N_{\text{jets}} = 2, n\text{Jets_DL1r_60} >= 1, tZ \text{ BDT} > 0.725$
2j tZ CR	$N_{\text{jets}} = 2, n\text{Jets_DL1r_60} >= 1, tZ \text{ BDT} < 0.725$

249 cutoff is arrived at by performing an Asimov fit with a variety of cutoffs, and selecting the value
 250 that produces the highest significance for the measurement of $WZ + b$.

251 The modeling in each region is validated by comparing data and MC predictions for various
 252 kinematic distributions. These plot are shown in figures 3-16.

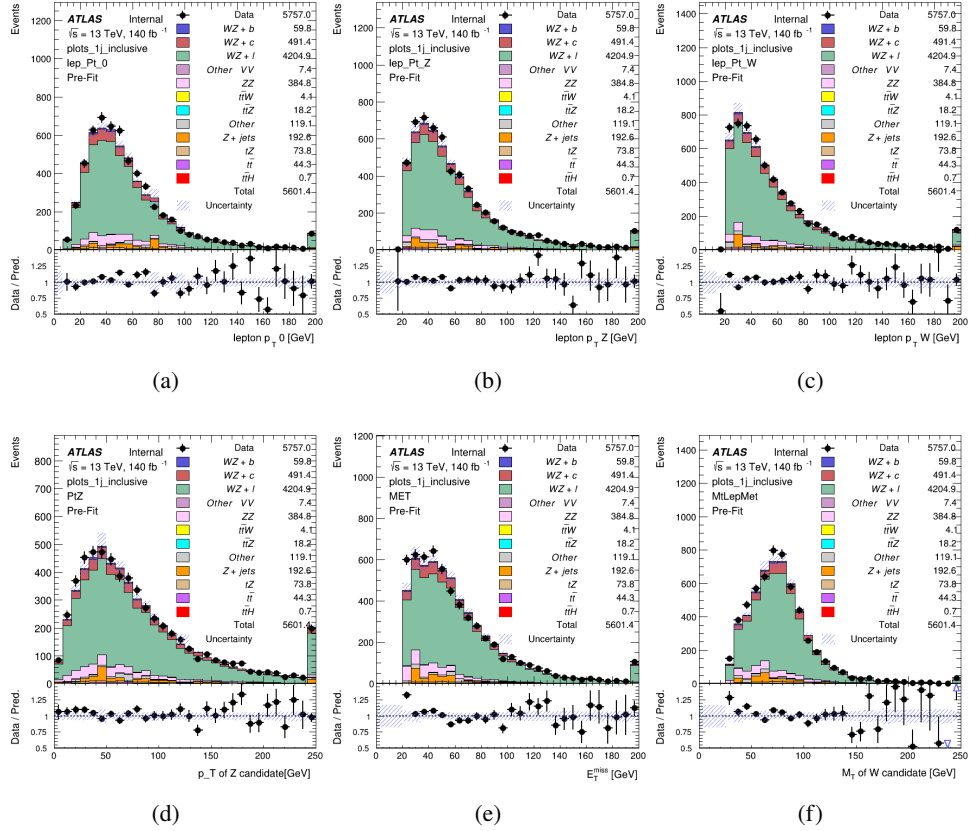
WZ Fit Region - 1j Inclusive

Figure 3: Comparisons between the data and MC distributions in the preselection region for (a) the p_T of the opposite sign lepton, (b) the p_T of the other lepton from the Z candidate, (c) the p_T of the lepton from the W candidate, (d) the p_T of the Z candidate, (e) the E_T^{miss} , and (f) the m_T of the W candidate.

WZ Fit Region - 1j < 85% WP

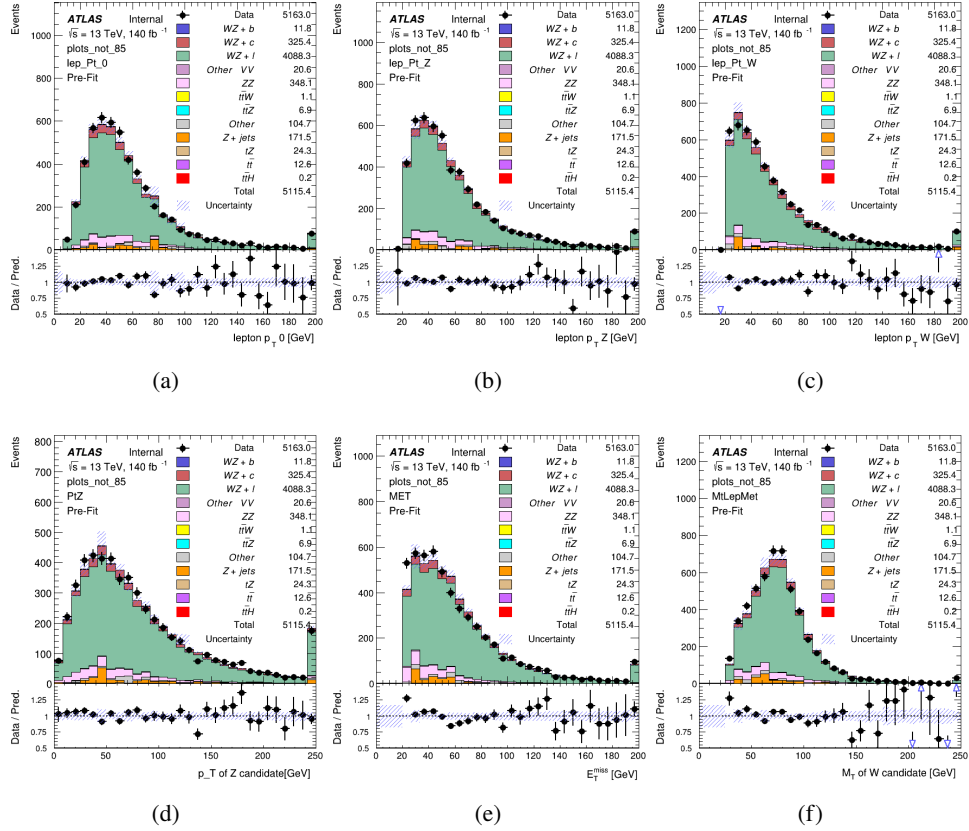


Figure 4: Comparisons between the data and MC distributions in the preselection region for (a) the p_T of the opposite sign lepton, (b) the p_T of the other lepton from the Z candidate, (c) the p_T of the lepton from the W candidate, (d) the p_T of the Z candidate, (e) the E_T^{miss} , and (f) the m_T of the W candidate.

WZ Fit Region - 1j 77-85% WP

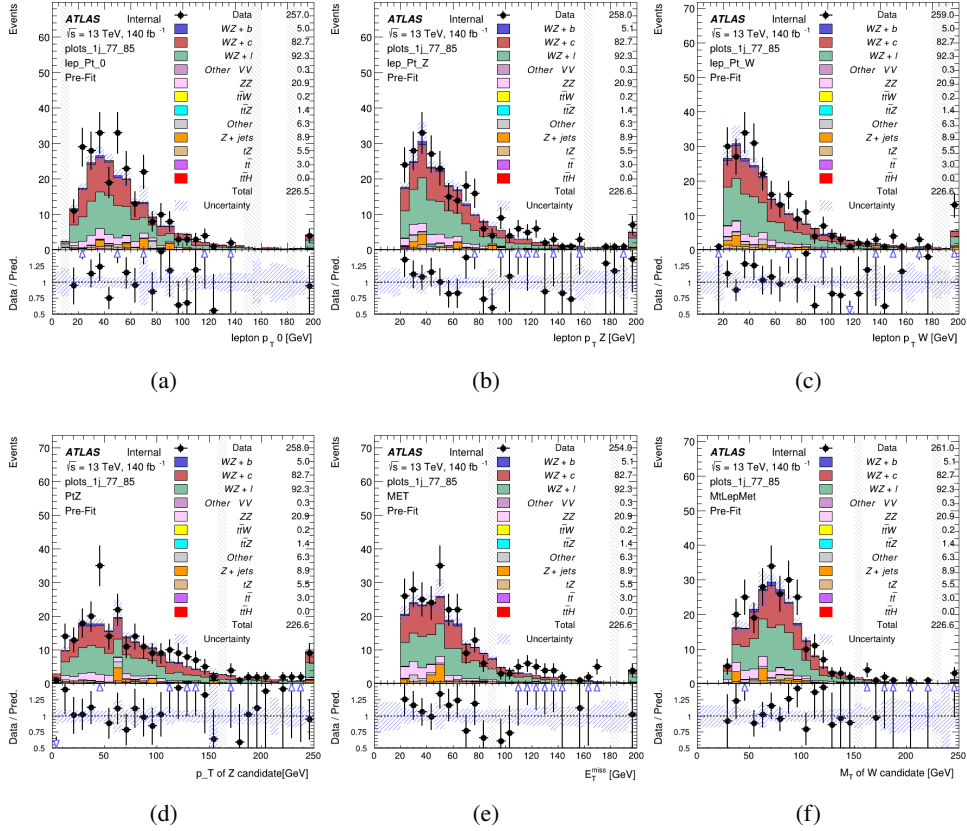


Figure 5: Comparisons between the data and MC distributions in the preselection region for (a) the p_T of the opposite sign lepton, (b) the p_T of the other lepton from the Z candidate, (c) the p_T of the lepton from the W candidate, (d) the p_T of the Z candidate, (e) the E_T^{miss} , and (f) the m_T of the W candidate.

WZ Fit Region - 1j 70-77% WP

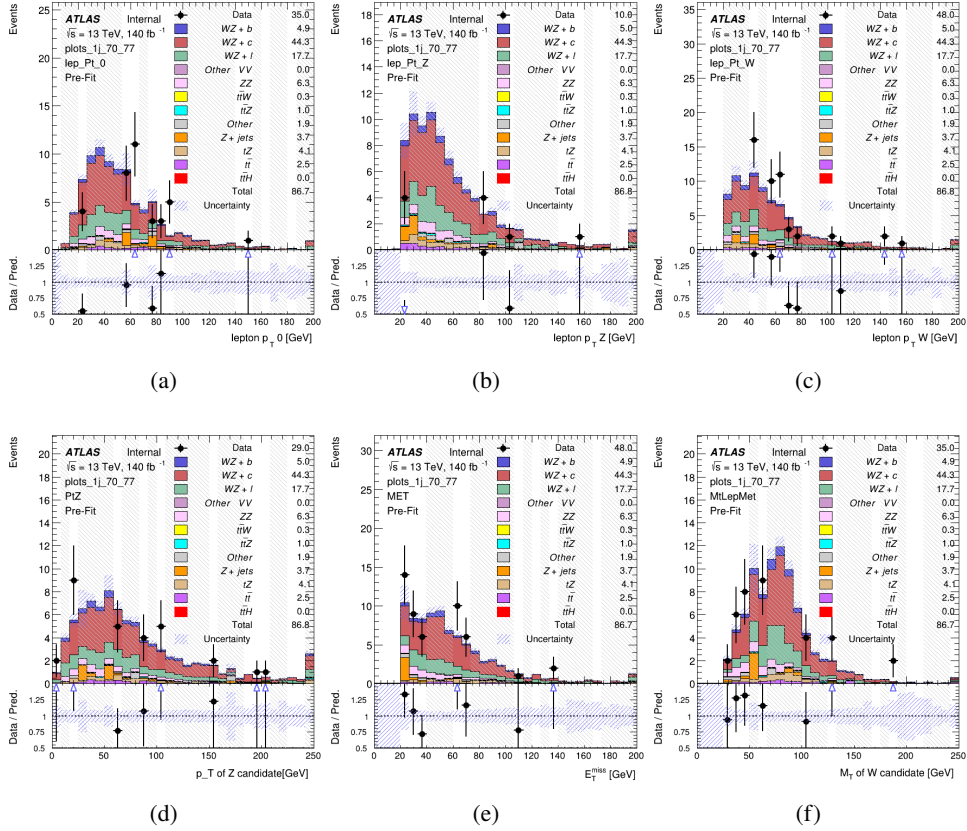


Figure 6: Comparisons between the data and MC distributions in the preselection region for (a) the p_T of the opposite sign lepton, (b) the p_T of the other lepton from the Z candidate, (c) the p_T of the lepton from the W candidate, (d) the p_T of the Z candidate, (e) the E_T^{miss} , and (f) the m_T of the W candidate.

WZ Fit Region - 1j 60-70% WP

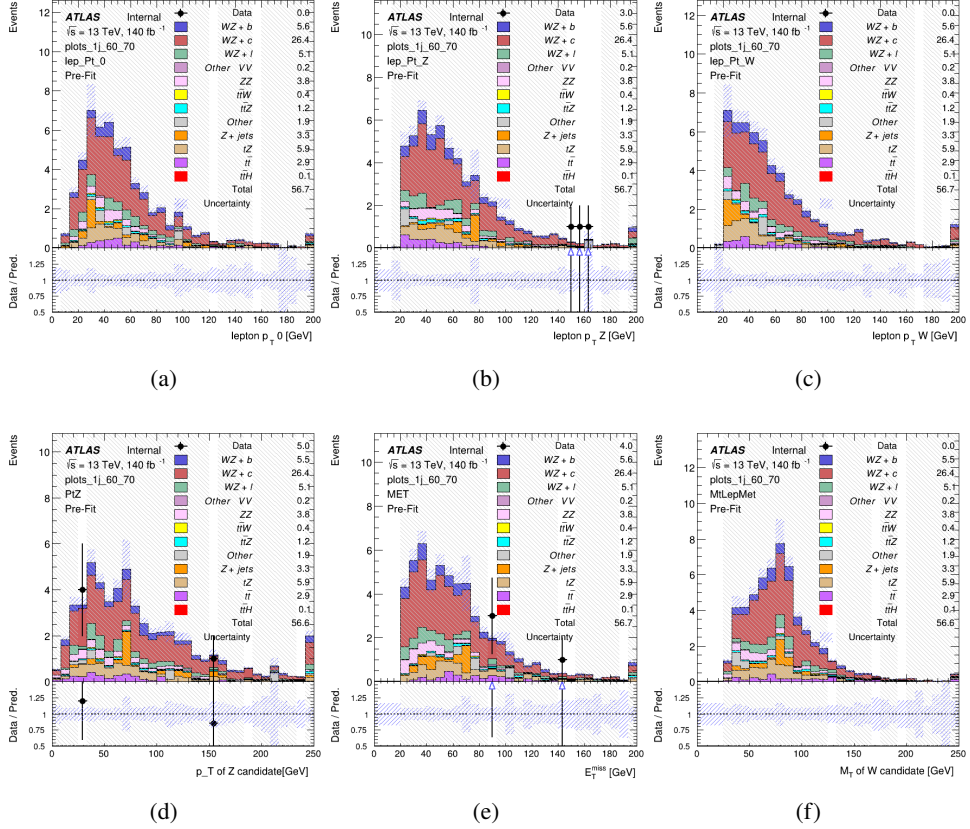


Figure 7: Comparisons between the data and MC distributions in the preselection region for (a) the p_T of the opposite sign lepton, (b) the p_T of the other lepton from the Z candidate, (c) the p_T of the lepton from the W candidate, (d) the p_T of the Z candidate, (e) the E_T^{miss} , and (f) the m_T of the W candidate.

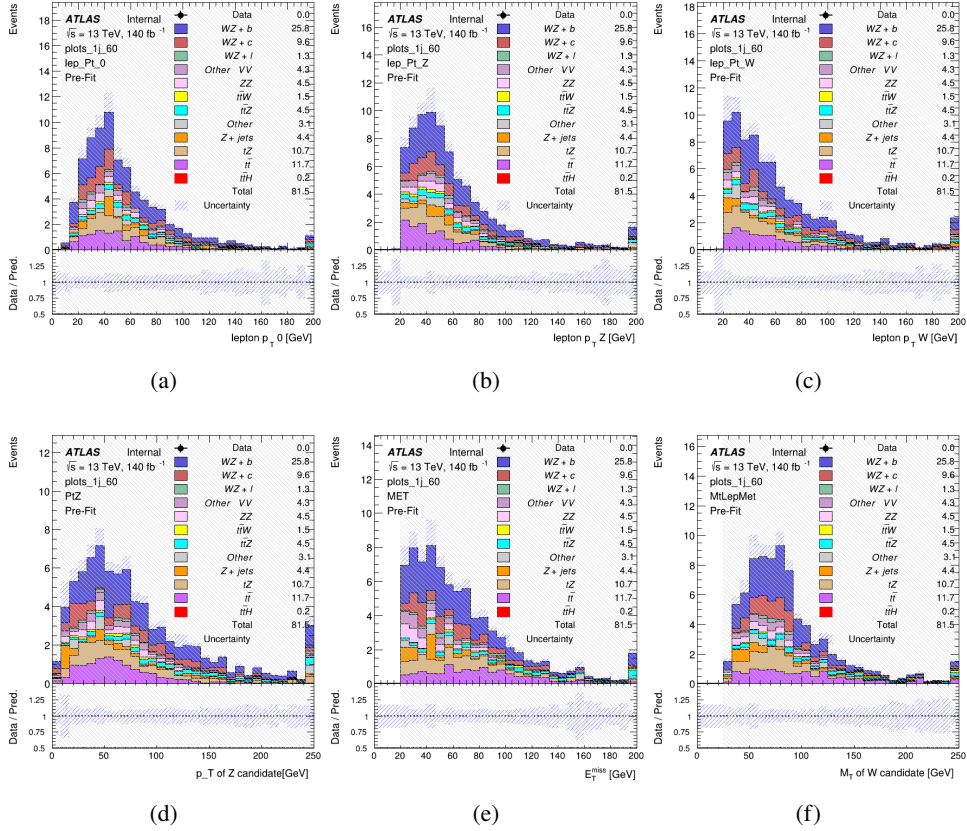
WZ Fit Region - 1j 60% WP

Figure 8: Comparisons between the data and MC distributions in the preselection region for (a) the p_T of the opposite sign lepton, (b) the p_T of the other lepton from the Z candidate, (c) the p_T of the lepton from the W candidate, (d) the p_T of the Z candidate, (e) the E_T^{miss} , and (f) the m_T of the W candidate.

WZ Fit Region - tZ-CR

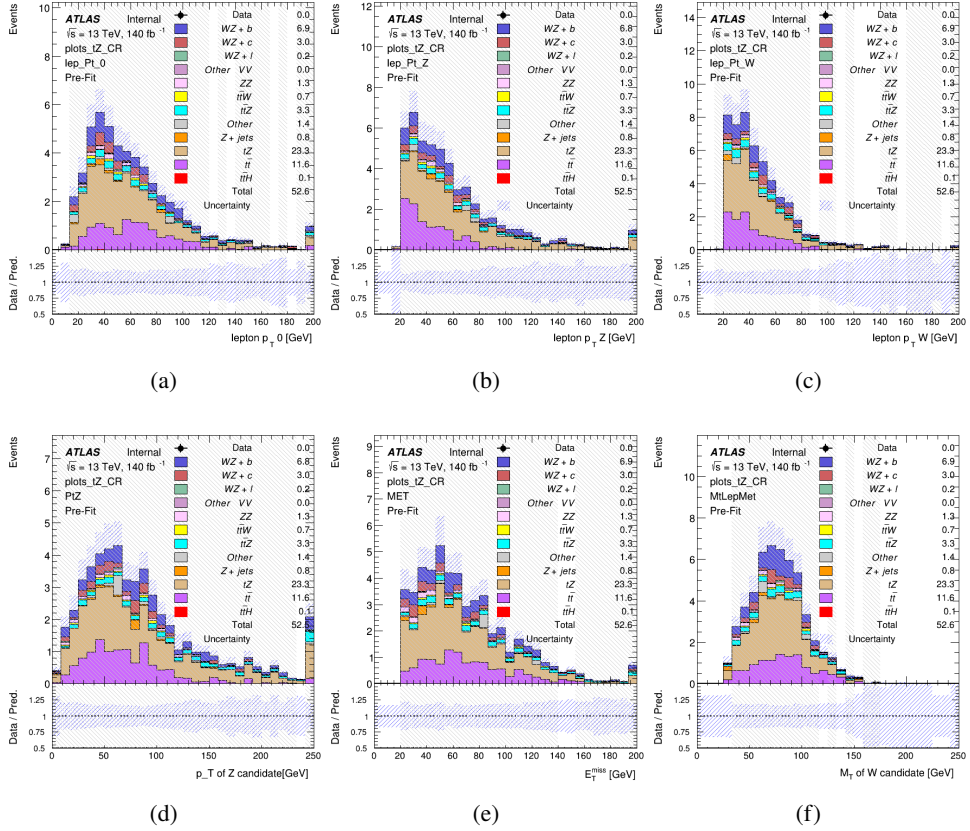


Figure 9: Comparisons between the data and MC distributions in the preselection region for (a) the p_T of the opposite sign lepton, (b) the p_T of the other lepton from the Z candidate, (c) the p_T of the lepton from the W candidate, (d) the p_T of the Z candidate, (e) the E_T^{miss} , and (f) the m_T of the W candidate.

WZ Fit Region - 2j Inclusive

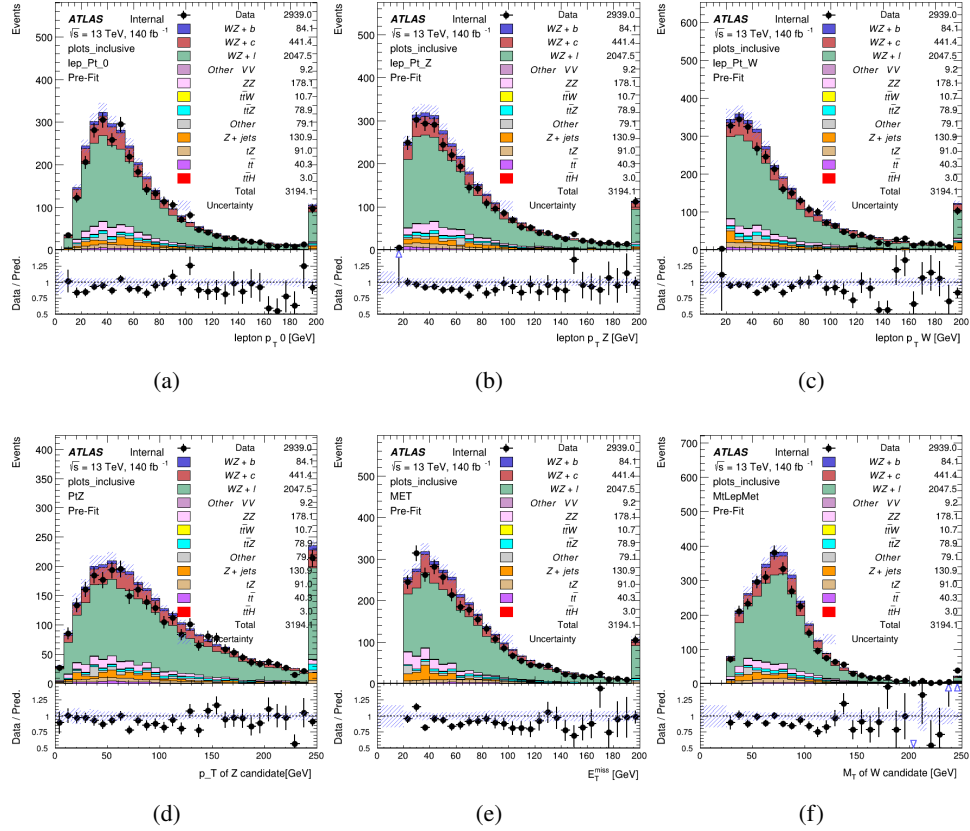


Figure 10: Comparisons between the data and MC distributions in the preselection region for (a) the p_T of the opposite sign lepton, (b) the p_T of the other lepton from the Z candidate, (c) the p_T of the lepton from the W candidate, (d) the p_T of the Z candidate, (e) the E_T^{miss} , and (f) the M_T of the W candidate.

WZ Fit Region - 2j < 85% WP

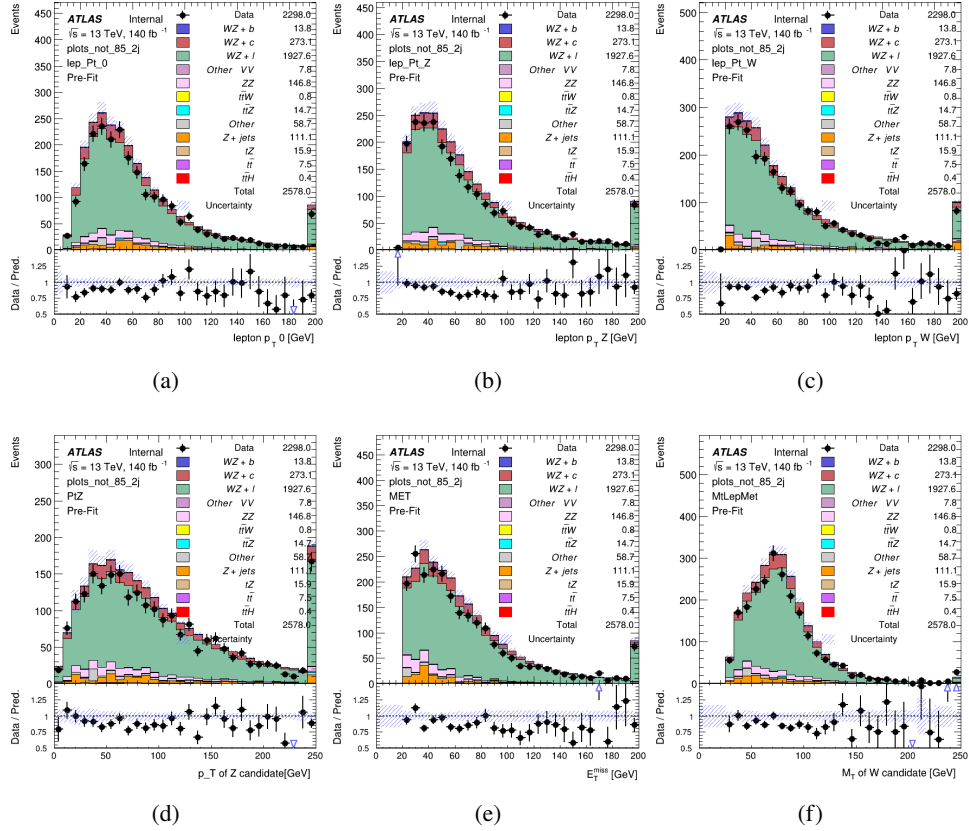


Figure 11: Comparisons between the data and MC distributions in the preselection region for (a) the p_T of the opposite sign lepton, (b) the p_T of the other lepton from the Z candidate, (c) the p_T of the lepton from the W candidate, (d) the p_T of the Z candidate, (e) the E_T^{miss} , and (f) the m_T of the W candidate.

WZ Fit Region - 2j 77-85% WP

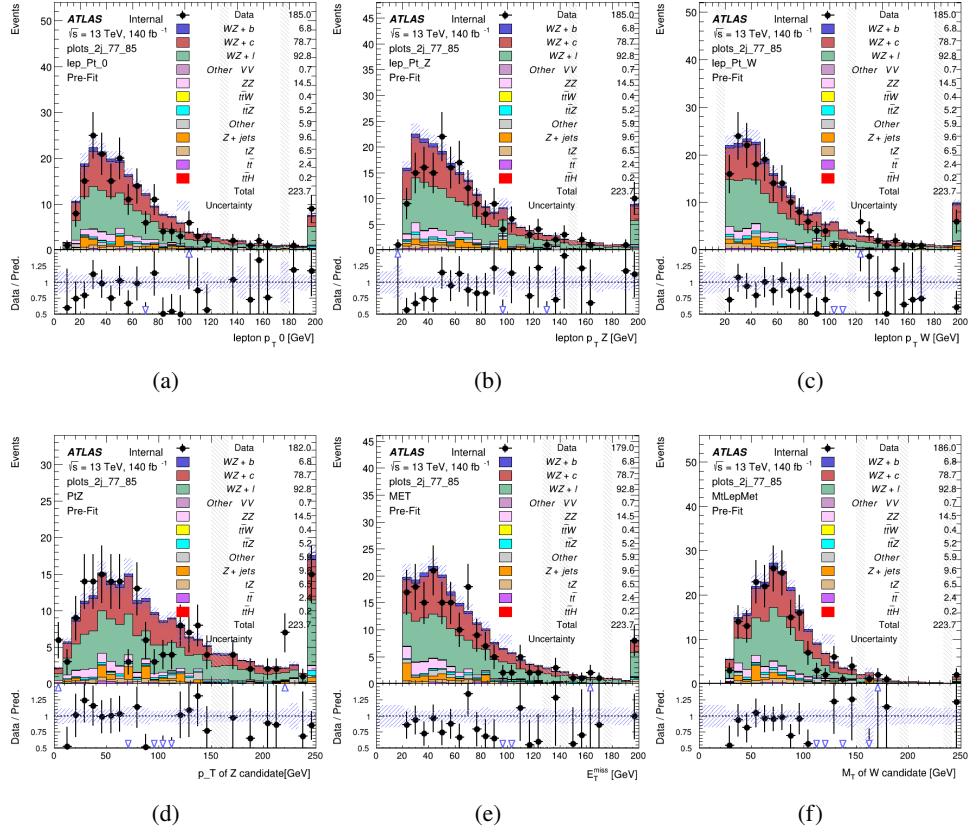


Figure 12: Comparisons between the data and MC distributions in the preselection region for (a) the p_T of the opposite sign lepton, (b) the p_T of the other lepton from the Z candidate, (c) the p_T of the lepton from the W candidate, (d) the p_T of the Z candidate, (e) the E_T^{miss} , and (f) the m_T of the W candidate.

WZ Fit Region - 2j 70-77% WP

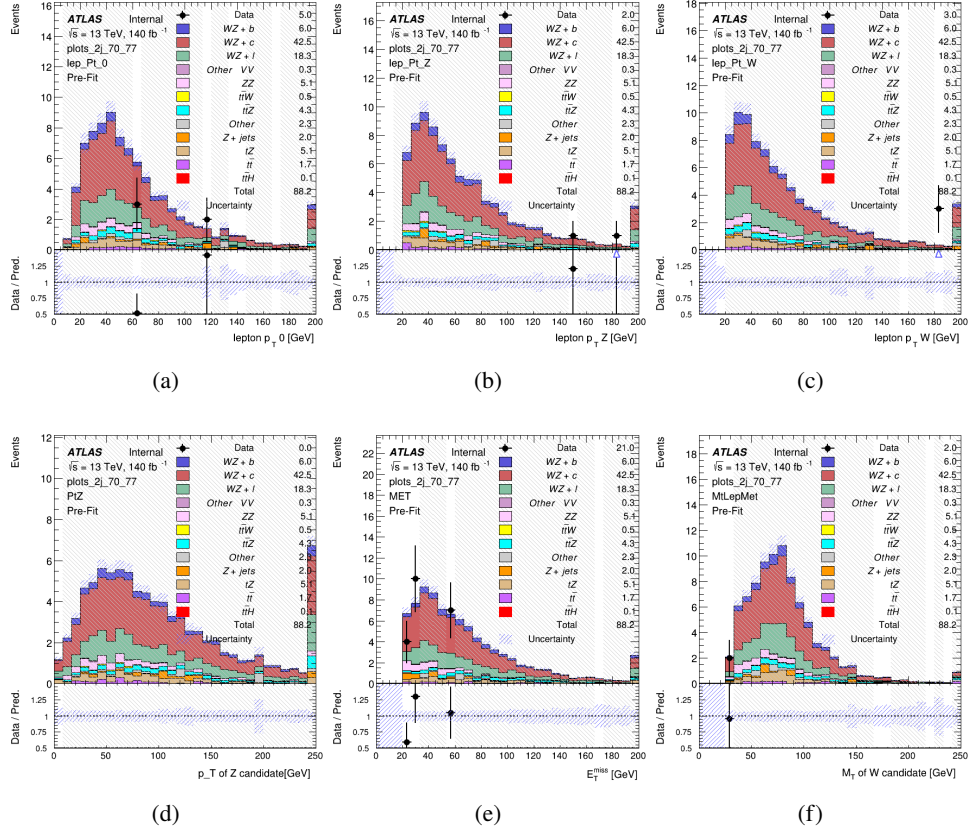


Figure 13: Comparisons between the data and MC distributions in the preselection region for (a) the p_T of the opposite sign lepton, (b) the p_T of the other lepton from the Z candidate, (c) the p_T of the lepton from the W candidate, (d) the p_T of the Z candidate, (e) the E_T^{miss} , and (f) the m_T of the W candidate.

WZ Fit Region - 2j 60-70% WP

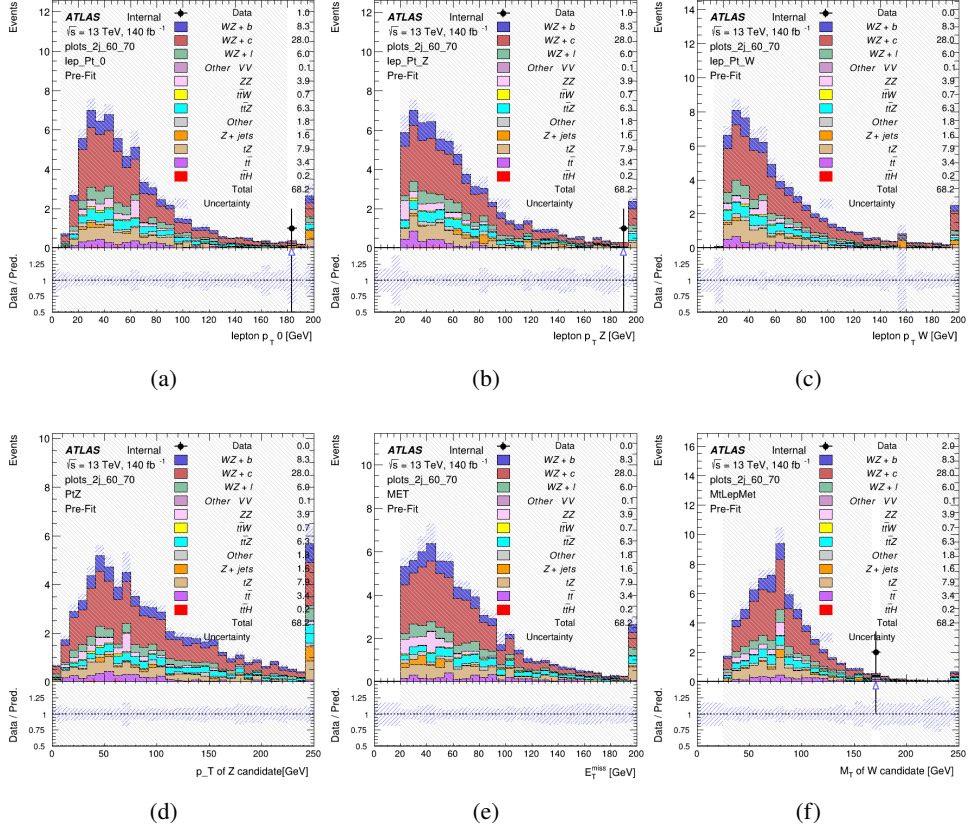


Figure 14: Comparisons between the data and MC distributions in the preselection region for (a) the p_T of the opposite sign lepton, (b) the p_T of the other lepton from the Z candidate, (c) the p_T of the lepton from the W candidate, (d) the p_T of the Z candidate, (e) the E_T^{miss} , and (f) the m_T of the W candidate.

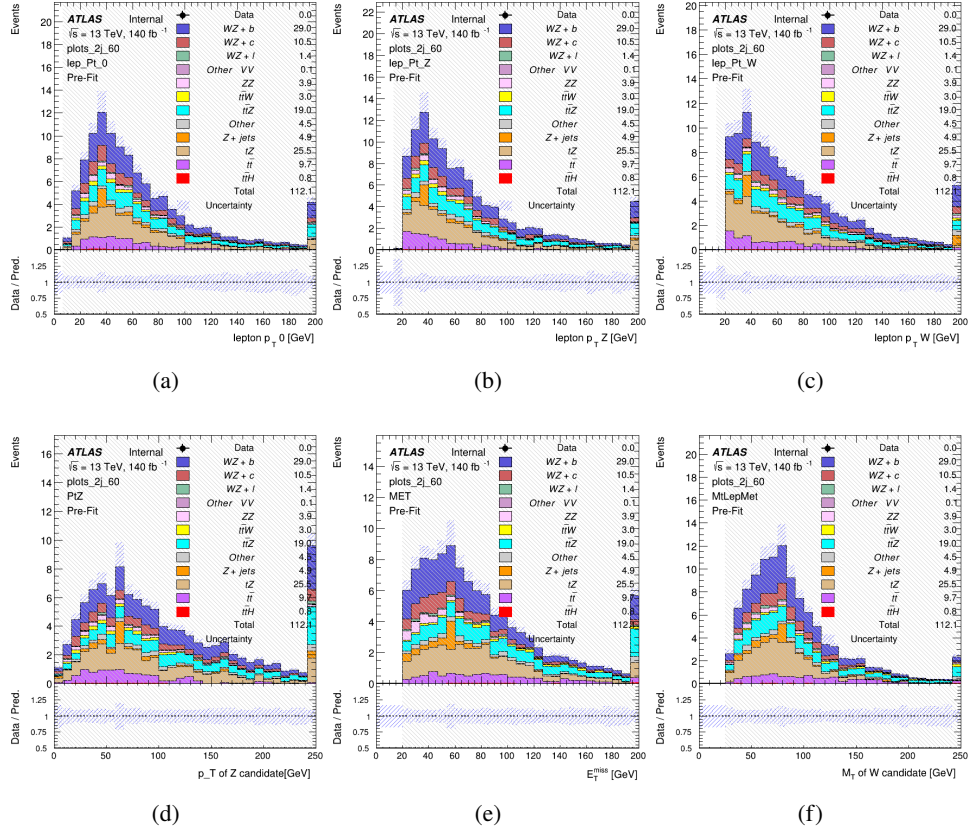
WZ Fit Region - 2j 60% WP

Figure 15: Comparisons between the data and MC distributions in the preselection region for (a) the p_T of the opposite sign lepton, (b) the p_T of the other lepton from the Z candidate, (c) the p_T of the lepton from the W candidate, (d) the p_T of the Z candidate, (e) the E_T^{miss} , and (f) the m_T of the W candidate.

WZ Fit Region - tZ-CR-2j

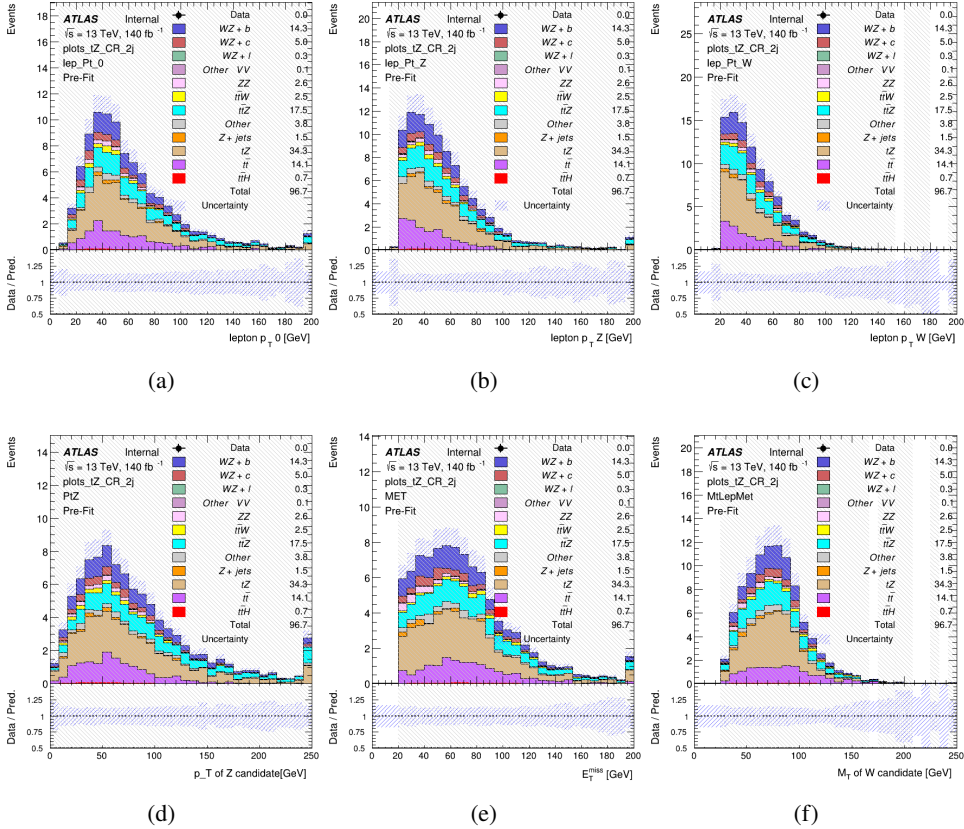


Figure 16: Comparisons between the data and MC distributions in the preselection region for (a) the p_T of the opposite sign lepton, (b) the p_T of the other lepton from the Z candidate, (c) the p_T of the lepton from the W candidate, (d) the p_T of the Z candidate, (e) the E_T^{miss} , and (f) the m_T of the W candidate.

5.3 Non-Prompt Lepton Estimation

Two processes act as sources of non-prompt leptons appear in the analysis: $t\bar{t}$ and $Z+jet$ production both produce two prompt leptons, and each contribute to the 3l region when an additional non-prompt lepton appears in the event. The contribution of these processes is estimated with Monte Carlo simulations, which are validated using enriched validation regions.

5.3.1 $t\bar{t}$ Validation

$t\bar{t}$ events can produce two prompt leptons from the decay of each of the tops. These top decays produce two b-quarks, the decay of which can produce additional non-prompt leptons, which occasionally pass the event preselection. In order to validate that the Monte Carlo accurately

262 simulates this process accurately, the MC prediction in a non-prompt $t\bar{t}$ enriched validation
263 region is compared to data.

264 The $t\bar{t}$ validation region is similar to the preselection region - three leptons meeting the criteria
265 described in section 5 are required, and the requirements on E_T^{miss} remain the same. However,
266 the selection requiring a lepton pair form a Z-candidate are reversed. Events where the invariant
267 mass of any two opposite sign, same flavor leptons falls within 10 GeV of 91.2 GeV are rejected.
268 This ensures the $t\bar{t}$ validation region is orthogonal to the preselection region.

269 Further, because the jet multiplicity of $t\bar{t}$ events tends to be higher than WZ, the number of jets
270 in each event is required to be greater than 1. As b-jets are almost invariably produced from top
271 decays, at least one b-tagged jet passing the 70% DL1r WP in each event is required. Various
272 kinematic plots of this region are shown in figure 17.

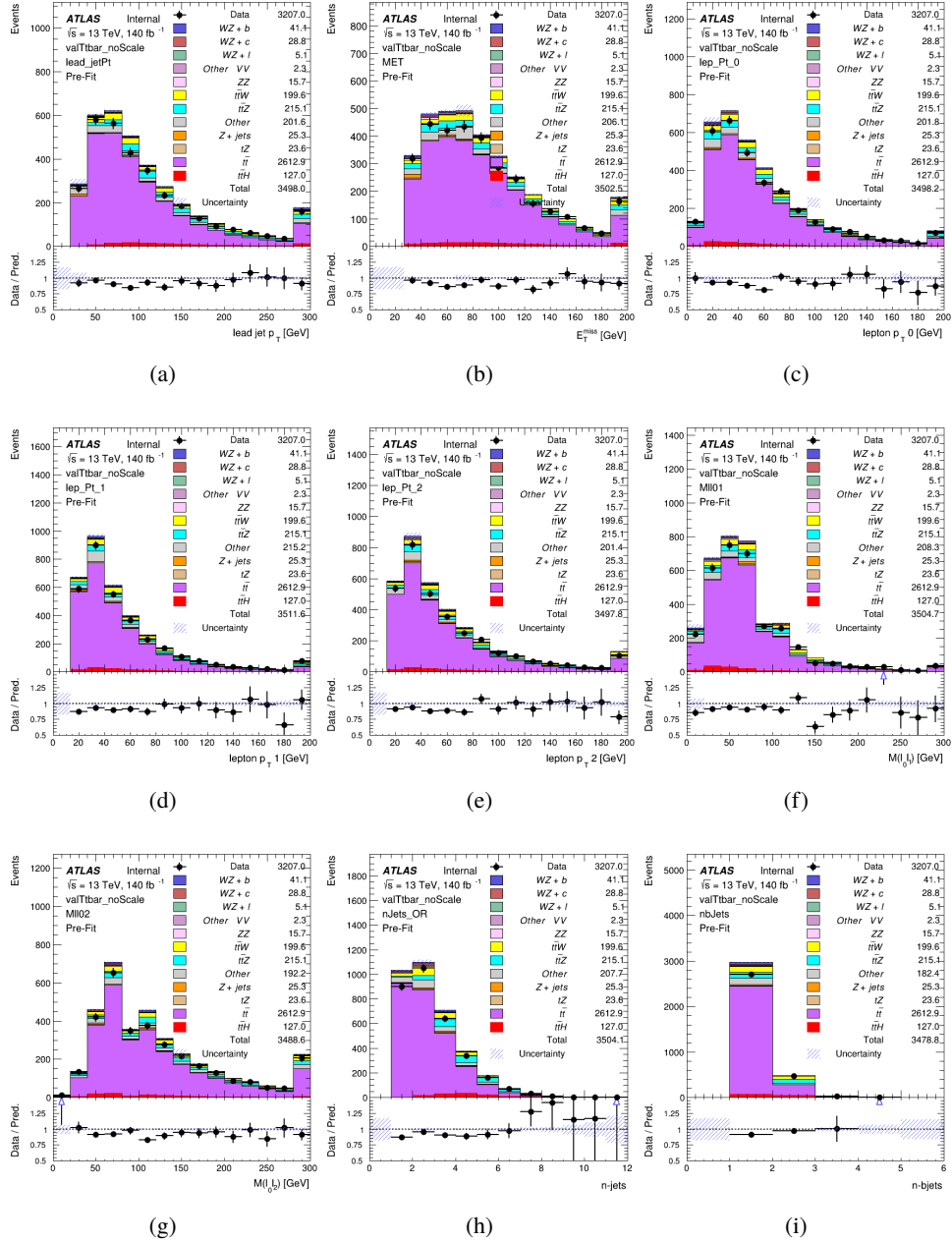


Figure 17: Comparisons between the data and MC distributions in the $t\bar{t}$ validation region for (a) the p_T of the leading jet, (b) the missing transverse energy, (c) the p_T of lepton 0, (d) p_T of lepton 1, (e) p_T of lepton 2, (f) the invariant mass of leptons 0 and 1, (g) the invariant mass of leptons 0 and 2, (h) the number of jets, (i) the number of b-tagged jets.

273 The shape of each distribution agrees quite well between data and MC, with a constant offset
274 between the two. This is accounted for by applying a constant correction factor of 0.883 to the $t\bar{t}$

275 MC prediction. Plots showing the kinematics of the $t\bar{t}$ VR after this correction factor has been
 276 applied are shown in figure 18.

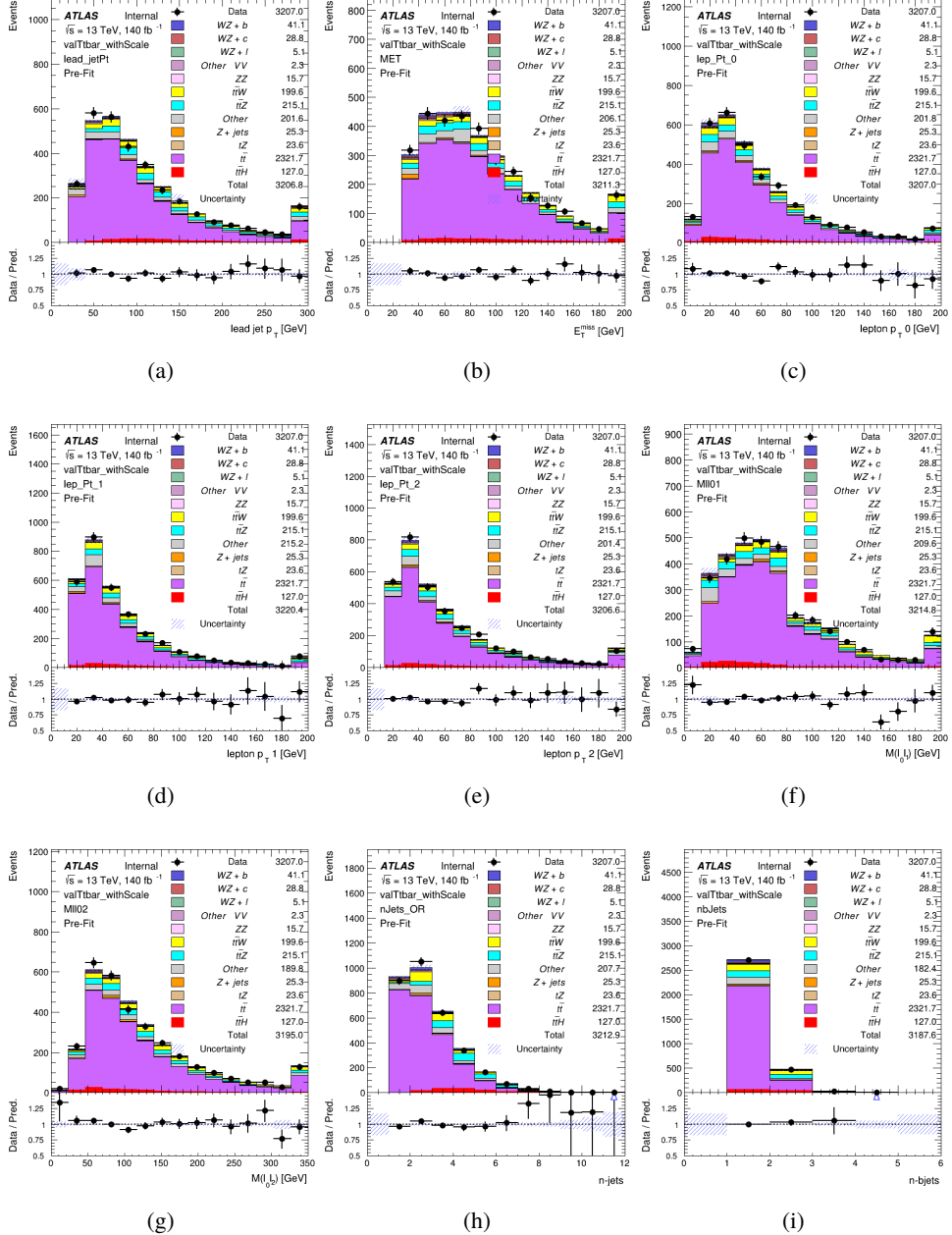


Figure 18: Comparisons between the data and MC distributions in the $t\bar{t}$ validation region after the correction factor has been applied for (a) the p_T of the leading jet, (b) the missing transverse energy, (c) the p_T of lepton 0, (d) p_T of lepton 1, (e) p_T of lepton 2, (f) the invariant mass of leptons 0 and 1, (g) the invariant mass of leptons 0 and 2, (h) the number of jets, (i) the number of b-tagged jets.

277 The modeling is further validated by looking at the yield in the $t\bar{t}$ VR for each DL1r WP, giving
 278 a clearer correspondence to the signal regions used in the fit. Each region shown in figure 22
 279 requires one or more jets pass the listed WP, with no jets passing the next highest WP.

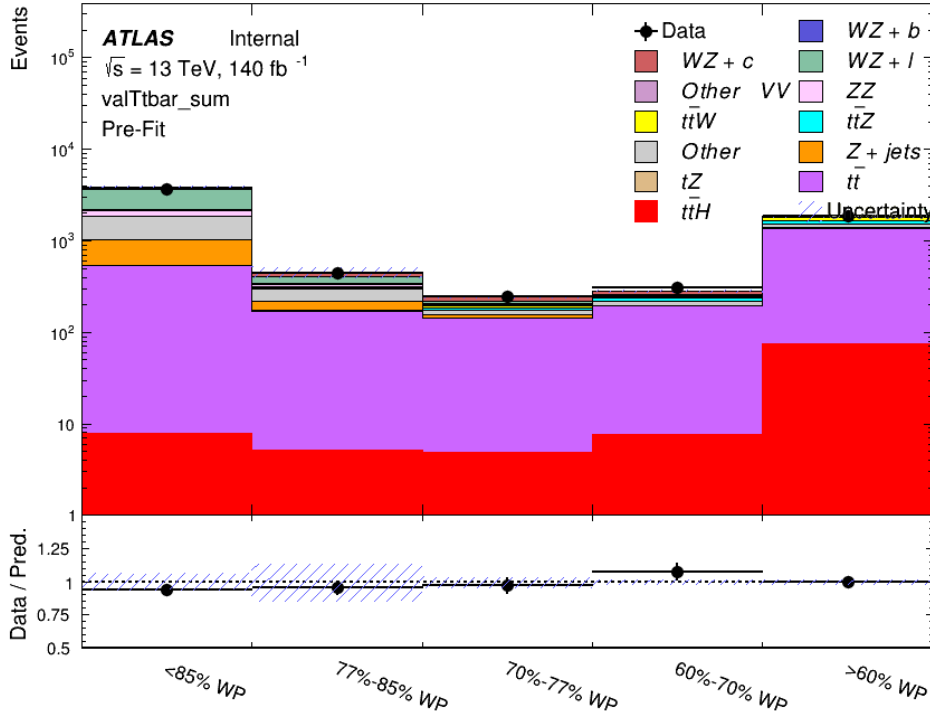


Figure 19: Data and MC comparisons for each DL1r WP for both 1-jet and 2-jet regions, after the $t\bar{t}$ VR selection and correction factor have been applied

280 As data and MC are found to agree within 10% for each of these working points, a 10% systematic
 281 uncertainty on the $t\bar{t}$ prediction is included for the analysis.

282 5.3.2 Z+jets Validation

283 Similar to $t\bar{t}$, a non-prompt Z+jets validation region is produced in order to validate the MC
 284 predictions. The lepton requirements remain the same as the preselection region. Because no
 285 neutrinos are present for this process, the E_T^{miss} cut is reversed, requiring $E_T^{\text{miss}} < 30 \text{ GeV}$. This
 286 also ensures this validation region is orthogonal to the preselection region. Further, the number
 287 of jets in each event is required to be greater than or equal to one. Various kinematic plots of this
 288 region are shown below. The general agreement between data and MC in each of these suggests
 289 that the non-prompt contribution of Z+jets is well modeled by Monte Carlo.

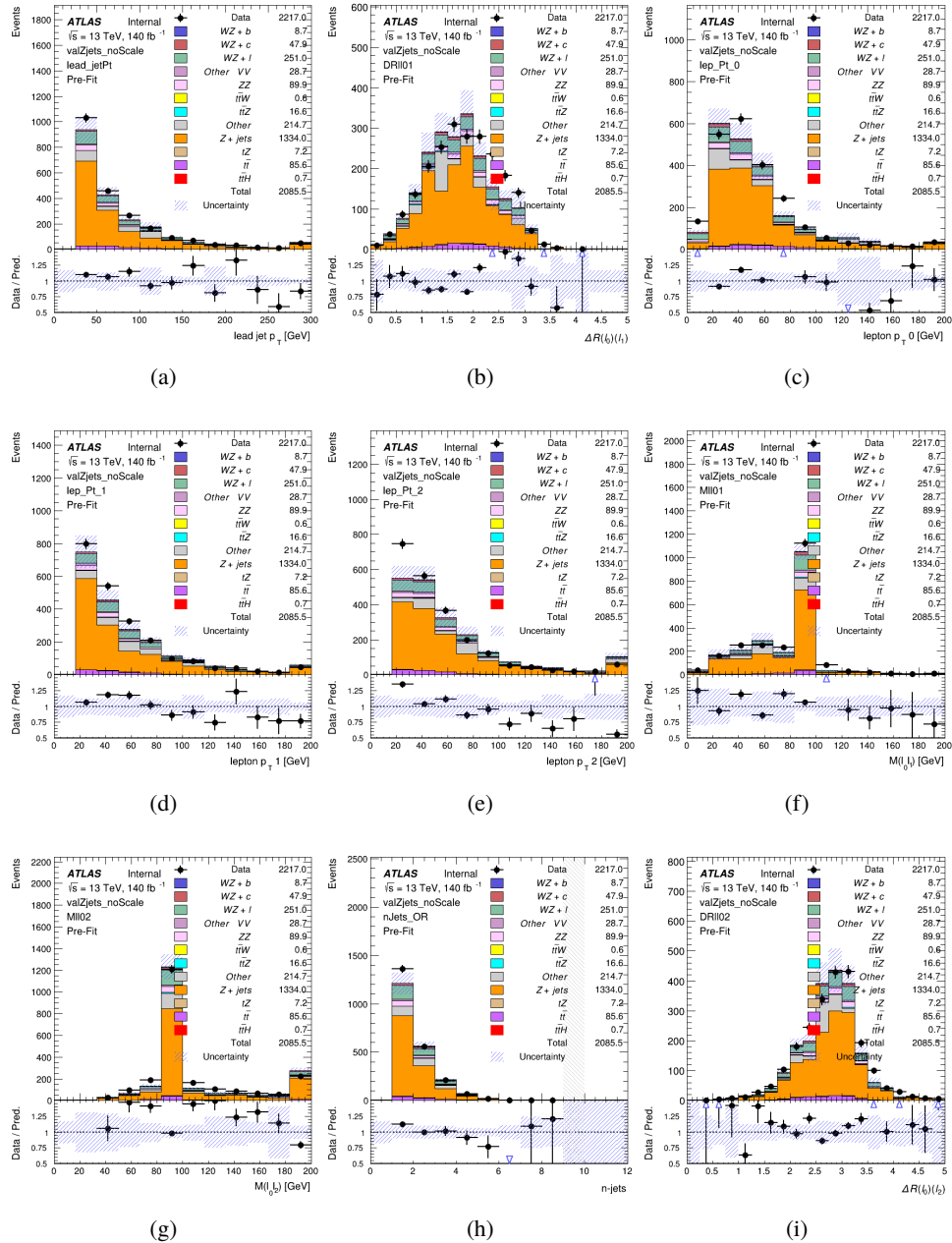


Figure 20: Comparisons between the data and MC distributions in the $Z + \text{jets}$ validation region for (a) the p_T of the leading jet, (b) ΔR between leptons 0 and 1, (c) the p_T of lepton 0, (d) p_T of lepton 1, (e) p_T of lepton 2, (f) the invariant mass of leptons 0 and 1, (g) the invariant mass of leptons 0 and 2, (h) the number of jets, (i) ΔR between leptons 0 and 2. Includes only statistical uncertainties

290 While there is general agreement between data and MC within statistical uncertainty, the shape

²⁹¹ of the p_T spectrum of lepton 2 is found to differ. To account for this discrepancy, a variable
²⁹² correction factor is applied to Z+jets. χ^2 minimization of the lepton 2 p_T spectrum is performed
²⁹³ to derive a correction factor of $1.53 - 6.6 * 10^{-6}(\text{lep_Pt_2})$. Kinematic plots of the Z + jets
²⁹⁴ validation region after this correction factor has been aplied are shown in figure 21.

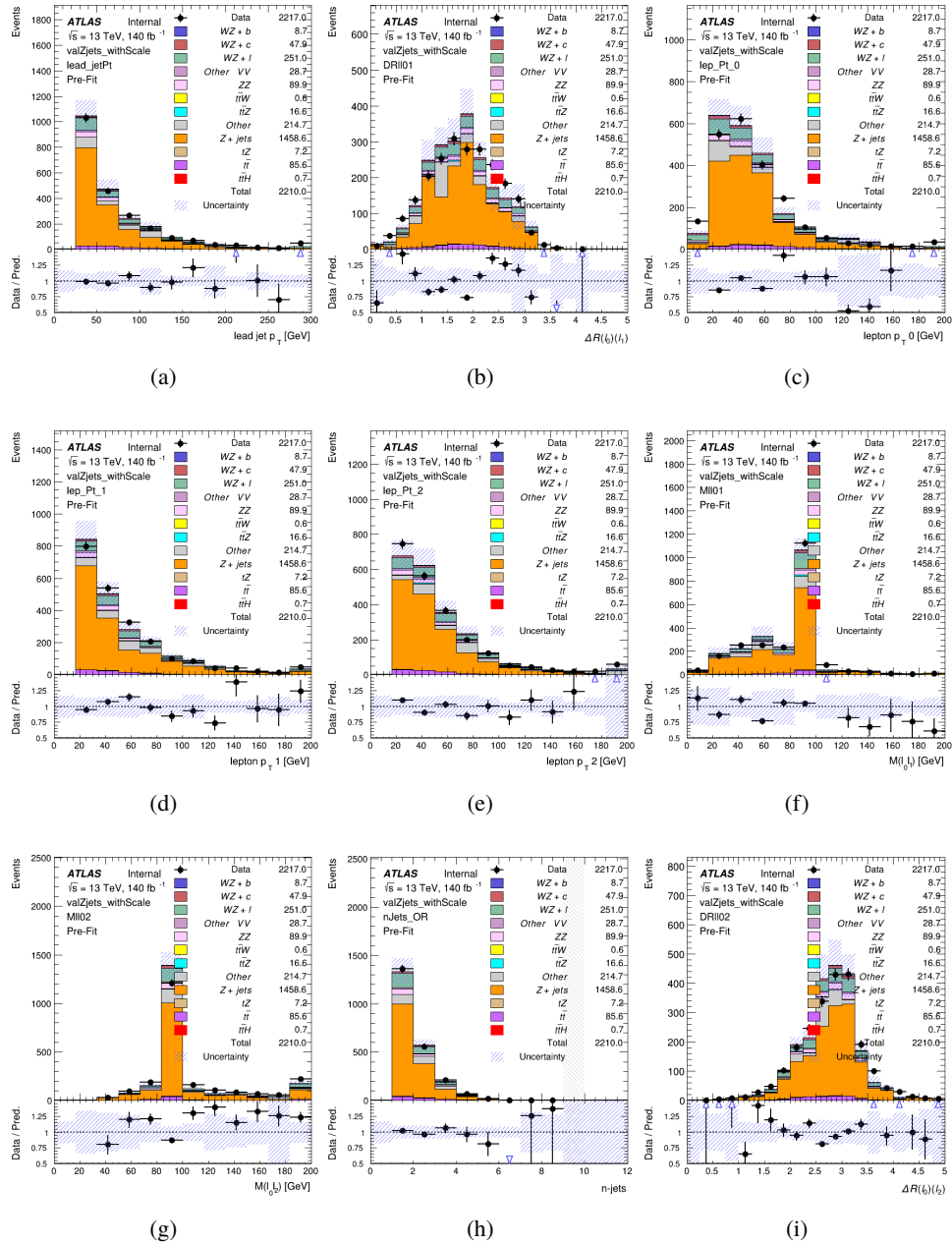


Figure 21: Comparisons between the data and MC distributions in the Z+jets validation region after the correction factor has been applied for (a) the p_T of the leading jet, (b) ΔR between leptons 0 and 1, (c) the p_T of lepton 0, (d) p_T of lepton 1, (e) p_T of lepton 2, (f) the invariant mass of leptons 0 and 1, (g) the invariant mass of leptons 0 and 2, (h) the number of jets, (i) ΔR between leptons 0 and 2

295 The modeling is further validated by looking at the yield in the Z+jets VR for each DL1r WP,

296 giving a clearer correspondence to the signal regions used in the fit. Each region shown in figure
 297 22 requires one or more jets pass the listed WP, with no jets passing the next highest WP.

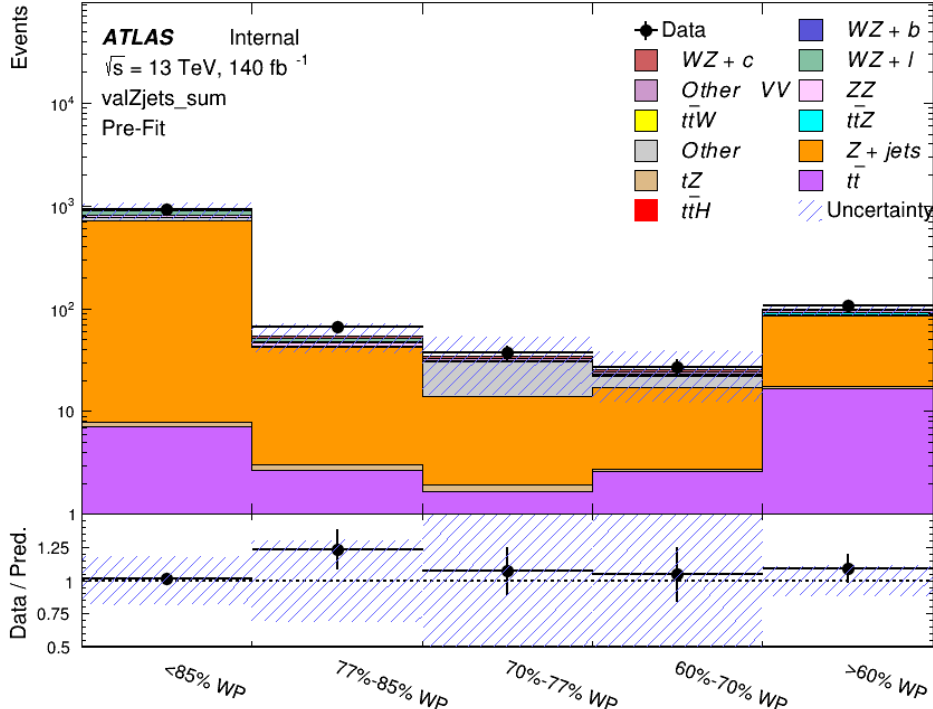


Figure 22: Data and MC comparisons for each DL1r WP for both 1-jet and 2-jet regions, after the Z+jets VR selection and correction factor have been applied

298 For each of the working points considered, the data falls within 20% of the MC prediction once
 299 this correction factor has been applied. Therefore, a 20% systematic uncertainty is applied to Z
 300 + jets in the analysis.

301 6 tZ Interference Studies and Separation Multivariate Analysis

302 Because it includes an on-shell Z boson as well as a b-jet and W from the top decay, tZ
 303 production represents an identical final state to WZ + b-jet. This implies the possibility of matrix
 304 level interference between these two processes not accounted for in the Monte Carlo simulations,
 305 which consider the two processes independently. Truth level studies are performed in order to
 306 estimate the impact of these interference effects.

307 Because tZ produces a final state identical to signal, it represents a predominant background in
 308 the most signal enriched regions. That is, the region with one jet passing the 60% DL1r WP.

309 Therefore, a boosted decision tree (BDT) algorithm is trained using TMVA [10] to separate WZ
310 + heavy flavor from tZ.

311 Separation between tZ and WZ + heavy flavor is achieved in part by reconstructing the invariant
312 mass of the top candidate, which clusters more closely to the top mass for tZ than WZ + heavy
313 flavor.

314 The result of this BDT is used to create a tZ enriched region in the fit, reducing its impact on the
315 measurement of WZ + heavy flavor.

316 **6.1 Interference Studies**

317 In order to estimate the matrix level interference effects between tZ and WZ + b-jet, two different
318 sets of simulations are produced using MadGraph 5 [Madgraph] - one which simulates these
319 two processes independently, and another where they are produced simultaneously, such that
320 interference effects are present. These two sets of samples are then compared, and the difference
321 between them can be taken to represent any interference effects.

322 MadGraph simulations of 10,000 tZ and 10,000 WZ + b-jet events are produced, along with
323 20,000 events where both are present, in the fiducial region where three leptons and at least one
324 jet are produced.

325 The kinematics of these samples are shown below:

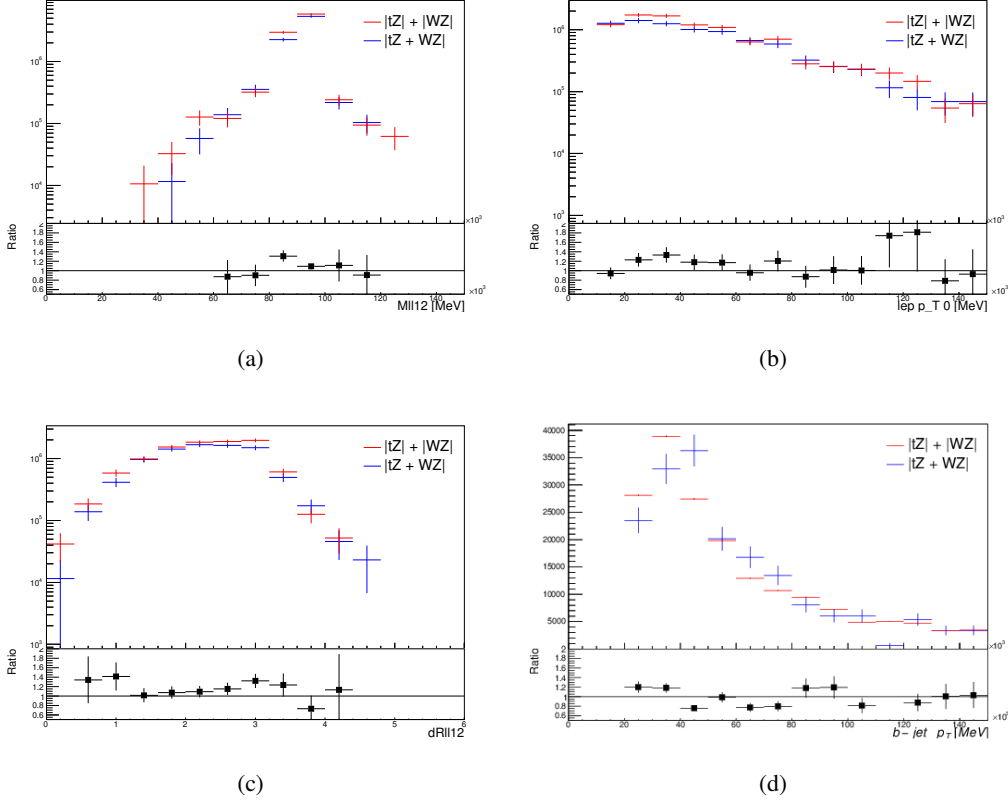


Figure 23: Comparisons between (a) the invariant mass of the Z-candidate, (b) the p_T of the leading lepton, (c) $\Delta(R)$ of the two leptons that form the Z-candidate, and (d) the p_T of the b-jet, for WZ and tZ events generated with interference effects (blue) and without interference effects (red).

6.2 Top Mass Reconstruction

The reconstruction of the top mass follows the procedure described in detail in section 6.1 of [11]. The mass of the top quark candidate is reconstructed from the jet, the lepton not included in the Z-candidate, and a reconstructed neutrino. In the case that there is one jet in the event, there is only possible b-jet candidate. For events with two jets, the jet with the highest DL1r score is used.

The neutrino from the W decay is expected to be the only source of E_T^{miss} . Therefore, the E_T and ϕ of the neutrino are taken from the E_T^{miss} measurement. This leaves the z-component of the neutrino momentum, p_{VZ} as the only unknown.

This unknown is solved for by taking the combined invariant mass of the lepton and neutrino to give the invariant mass of the W boson:

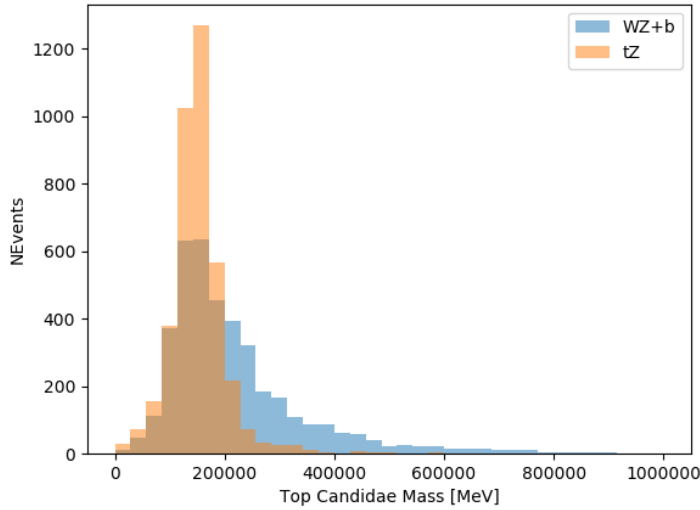


Figure 24: Reconstructed top mass distributions for tZ and WZ + b, measured in MeV.

$$^{337} \quad (p_l + p_\nu)^2 = m_W^2$$

³³⁸ Expanding this out into components, this equation gives:

$$^{339} \quad \sqrt{p_{T\nu}^2 + p_{z\nu}^2} E_l = \frac{m_W^2 - m_l^2}{2} + p_{T\nu}(p_{lx}\cos\phi_\nu + p_{ly}\sin\phi_\nu) + p_{lz}p_{\nu z}$$

³⁴⁰ This equation gives two solutions for $p_{\nu z}$. For cases where only one of these solutions is real,
³⁴¹ that is taken as the value of $p_{\nu z}$. For instances with two real solutions, the one which is shown
³⁴² to be correct in the largest fraction of simulations is taken. For cases when no real solution is
³⁴³ found, often because of detector effects, the value of E_T^{miss} is varied in decreasing increments of
³⁴⁴ 100 MeV until a real solution is found.

³⁴⁵ The reconstructed top mass distribution for tZ and WZ + b can be seen in figure 24.

³⁴⁶ 6.3 tZ BDT

³⁴⁷ A Boosted Decision Tree (BDT), specifically XGBoost [[xgboost_cite](#)], is used to provide separation
³⁴⁸ between tZ and WZ+b. The following kinematic variables are used as inputs:

- ³⁴⁹ • The invariant mass of the reconstructed top candidate
- ³⁵⁰ • p_T of each of the leptons, jet
- ³⁵¹ • The invariant mass of each combination of lepton pairs, $M(l\bar{l})$

- 352 • E_T^{miss}
 353 • Distance between each combination of leptons, $\Delta R(l_1 l_2)$
 354 • Distance between each lepton and the jet, $\Delta R(l_j)$

355 The training samples included only events meeting the requirements of the 1-jet, >60% region,
 356 i.e. passing all the selection described in section 5 and having exactly one jet which passes the
 357 tightest (60%) DL1r working point.

358 The distributions of a few of these features for both signal and background is shown in figure
 359 25.

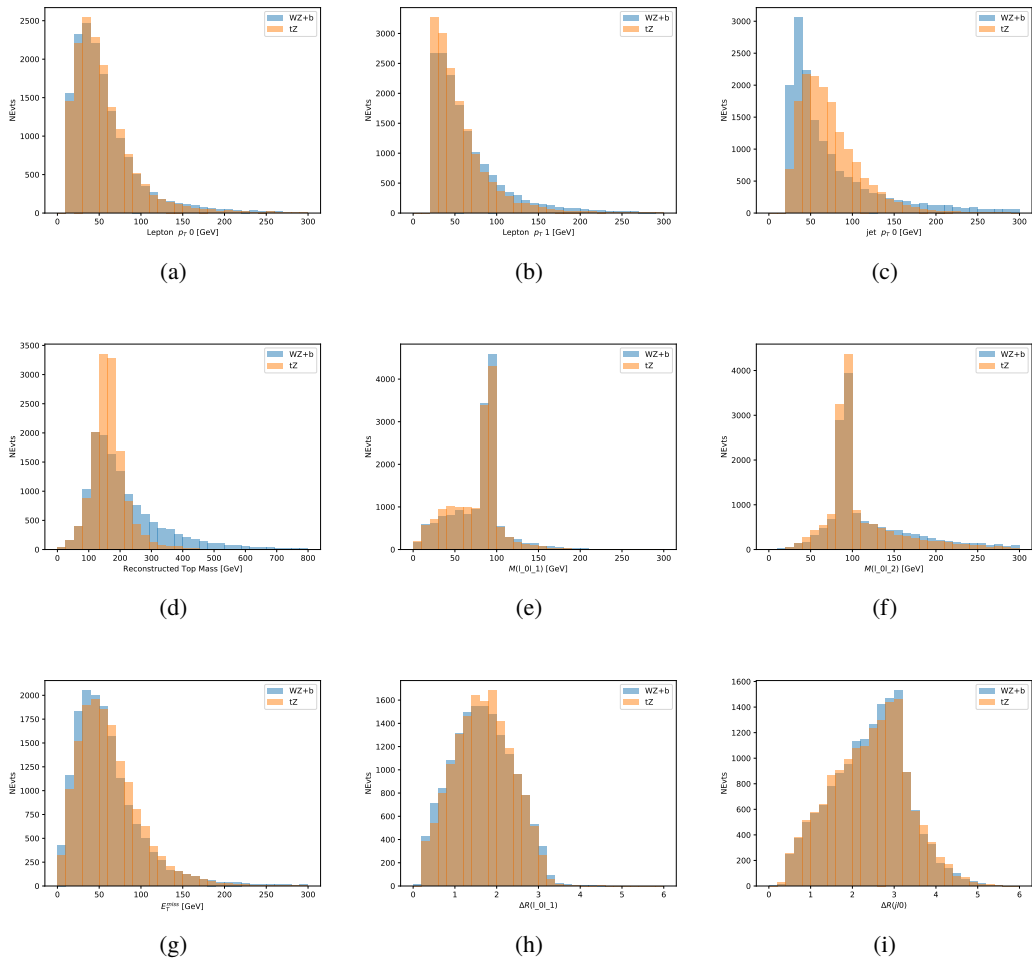


Figure 25: Distribution of input features of the BDT for signal (WZ) and background (tZ). Both are scaled to an equal number of events. (a), (b) and (c) show the p_T of lepton 0, lepton 1, and the jet, (d) show the reconstructed top mass, (e) and (f) show the invariant mass of leptons 0 and 1, leptons 0 and 2. (g) shows the E_T^{miss} of each event. (h) and (i) show the ΔR between lepton 0 and lepton 1, and the jet.

360 A sample of 20,000 background (tZ) and signal ($WZ+b$) Monte Carlo events are used to train
 361 the BDT. And additional 5,000 events are reserved for testing the model, in order to prevent
 362 over-fitting. A total of 750 decision trees with a maximum depth of 6 branches are used to build
 363 the model. These parameters are chosen empirically, by training several models with different
 364 parameters and selecting the one that gave the best separation for the test sample.

365 The results of the BDT training are shown in figure 26. The output scores for both signal and
 366 background events is shown on the left. The right shows the receiving operating characteristic
 367 (ROC) curve that results from the MVA. The ROC curve represents the background rejection
 368 as a function of signal efficiency, where each point on the curve represents a different response
 369 score. The ROC curve of the BDT is compared to the performance of using an optimal set of flat
 370 selections on the same set of input variables.

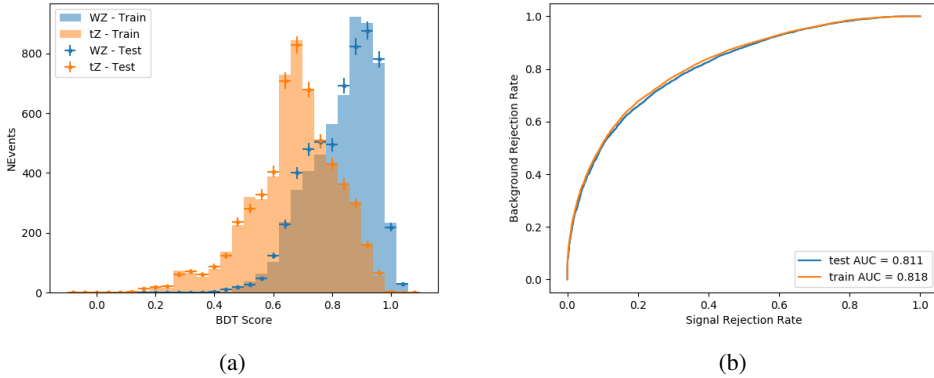


Figure 26: Distribution of the BDT response for signal and background events on the left, the ROC curve for the BDT on the right.

371 The relative important of each input feature in the model, measured by how often they appeared
 372 in the decision trees, is shown in figure 27.

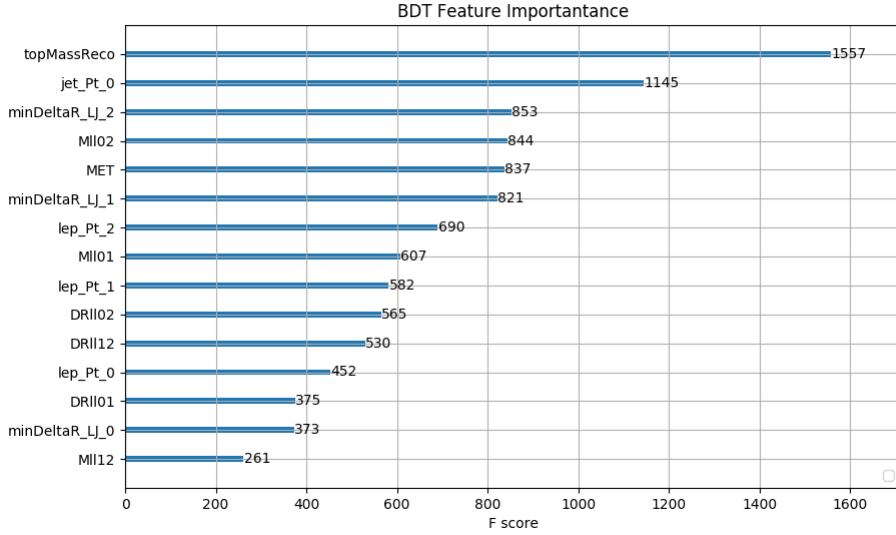


Figure 27: Relative importance of each input feature in the model.

373 These results suggest that some amount of separation can be achieved between these two pro-
 374 cesses, with a high BDT score selecting a set of events that is pure in $WZ + b$.

375 7 Systematic Uncertainties

376 The systematic uncertainties that are considered are summarized in table 9. These are imple-
 377 mented in the fit either as a normalization factors or as a shape variation or both in the signal
 378 and background estimations. The numerical impact of each of these uncertainties is outlined in
 379 section 8.

380 The uncertainty in the combined integrated luminosity is derived from a calibration of the
 381 luminosity scale performed for 13 TeV proton-proton collisions [12], [LUCID2].

382 The experimental uncertainties are related to the reconstruction and identification of light leptons
 383 and b-tagging of jets, and to the reconstruction of E_T^{miss} . The sources which contribute to the
 384 uncertainty in the jet energy scale [13] are decomposed into uncorrelated components and treated
 385 as independent sources in the analysis.

386 The uncertainties in the b-tagging efficiencies measured in dedicated calibration analyses [14] are
 387 also decomposed into uncorrelated components. The large number of components for b-tagging
 388 is due to the calibration of the distribution of the MVA discriminant.

389 The systematic uncertainties associated with the signal and background processes are accounted
 390 for by varying the cross-section of each process within its uncertainty.

Table 9: Sources of systematic uncertainty considered in the analysis.

Systematic uncertainty	Components
Luminosity	1
Pileup reweighting	1
Physics Objects	
Electron	6
Muon	15
Jet energy scale and resolution	28
Jet vertex fraction	1
Jet flavor tagging	131
E_T^{miss}	3
Total (Experimental)	186
Background Modeling	
Cross section	24
Renormalization and factorization scales	10
Parton shower and hadronization model	2
Shower tune	4
Total (Signal and background modeling)	40
Total (Overall)	226

³⁹¹ The full list of systematic uncertainties considered in the analysis is summarized in tables 10, 11
³⁹² and 12.

³⁹³

Experimental Systematics on Leptons and E_T^{miss}			
Type	Description	Systematics Name	Application
Trigger			
Scale Factors	Trigger Efficiency	lepSFTrigTight_MU(EL)_SF_Trigger_STAT(SYST)	Event Weight
Muons			
Efficiencies	Reconstruction and Identification	lepSFObjTight_MU_SF_ID_STAT(SYST)	Event Weight
	Isolation	lepSFObjTight_MU_SF_Isol_STAT(SYST)	Event Weight
	Track To Vertex Association	lepSFObjTight_MU_SF_TTVA_STAT(SYST)	Event Weight
p_T Scale	p_T Scale	MUONS_SCALE	p_T Correction
Resolution	Inner Detector Energy Resolution	MUONS_ID	p_T Correction
	Muon Spectrometer Energy Resolution	MUONS_MS	p_T Correction
Electrons			
Efficiencies	Reconstruction	lepSFObjTight_EL_SF_ID	Event Weight
	Identification	lepSFObjTight_EL_SF_Reco	Event Weight
	Isolation	lepSFObjTight_EL_SF_Isol	Event Weight
Scale Factor	Energy Scale	EG_SCALE_ALL	Energy Correction
Resolution	Energy Resolution	EG_RESOLUTION_ALL	Energy Correction
E_T^{miss}			
Soft Tracks Terms	Resolution	MET_SoftTrk_ResoPerp	p_T Correction
	Resolution	MET_SoftTrk_ResoPara	p_T Correction
	Scale	MET_SoftTrk_ScaleUp	p_T Correction
	Scale	MET_SoftTrk_ScaleDown	p_T Correction

Table 10: Summary of experimental systematics considered for leptons and E_T^{miss} . Includes type, description, name of systematic as used in the fit, and mode of application. The mode of application indicates the systematic evaluation, e.g. as an overall event re-weighting (Event Weight) or rescaling (p_T Correction).

Experimental Systematics on Jets			
Type	Origin	Systematics Name	Application
Jet Vertex Tagger		JVT	Event Weight
Energy Scale	Calibration Method	JET_21NP_ JET_EffectiveNP_1-19	p_T Correction p_T Correction
	η inter-calibration	JET_EtaIntercalibration_Modelling JET_EtaIntercalibration_NonClosure JET_EtaIntercalibration_TotalStat	p_T Correction p_T Correction p_T Correction
	High p_T jets	JET_SingleParticle_HighPt	p_T Correction
23rd January 2021 – PU Up	Pileup	JET_Pileup_OffsetNPV JET_Pileup_OffsetMu JET_Pileup_PtTerm JET_Pileup_RhoTopology	p_T Correction p_T Correction p_T Correction p_T Correction
		JET_PunchThrough_MC15	p_T Correction
		JET_Flavor_Response JET_BJES_Response JET_Flavor_Composition	p_T Correction p_T Correction p_T Correction
	Flavour		

Experimental Systematics on b-tagging		
Type	Origin	Systematic Name
Scale Factors	DL1r b-tagger efficiency on b originated jets in bins of η	DL1r_Continuous_EventWeight_B0-29
	DL1r b-tagger efficiency on c originated jets in bins of η	DL1r_Continuous_EventWeight_C0-19
	DL1r b-tagger efficiency on light flavoured originated jets in bins of η and p_T	DL1r_Continuous_EventWeight_Light0-79
	DL1r b-tagger extrapolation efficiency	DL1r_Continuous_EventWeight_extrapolation DL1r_Continuous_EventWeight_extrapolation_from_charm

Table 12: Summary of experimental systematics to be included for b-tagging of jets in the analysis, using the continuous DL1r tagging algorithm. All of the b-tagging related systematics are applied as event weights. From left: type, description, and the name of systematic used in the fit.

³⁹⁴ The cross-section uncertainties applied to background estimates are summarized in table 13.

Process	X-section [%]
tZ	+36 -31
t̄t H (aMC@NLO+Pythia8)	QCD Scale: +5.8 -9.2 PDF(+ α_S): ± 3.6
t̄t Z (aMC@NLO+Pythia8)	QCD Scale: +9.6 -11.3 PDF(+ α_S): ± 4
t̄t W (aMC@NLO+Pythia8)	QCD Scale: +12.9 -11.5 PDF(+ α_S): ± 3.4
VV + b/charm (Sherpa 2.2.1)	± 50
VV + light (Sherpa 2.2.1)	± 6
t̄t	± 20 placeholder
Z + jets	± 25 placeholder
Others	± 50

Table 13: Summary of theoretical uncertainties for MC prediction of backgrounds in the analysis.

³⁹⁵ 8 Results

³⁹⁶ A separate maximum-likelihood fit is performed over the 1-jet and 2-jet fit regions in order to
³⁹⁷ extract the best-fit value of the WZ + b-jet and WZ + charm jet contributions. The WZ + b,

398 WZ + charm and WZ + light contributions are allowed to float, with the remaining background
 399 contributions are held fixed. **The current fit strategy treats the WZ + b-jet contribution as**
 400 **the parameter of interest, with the normalization of the WZ + charm and the WZ + light**
 401 **contributions taken as systematic uncertainties. This could however be adjusted, depending**
 402 **on whether it is decided the goal of the analysis should be to measure WZ+b specifically or**
 403 **WZ + heavy flavor overall.** The result of the fit is used to extract the cross-section of WZ +
 404 heavy-flavor production.

405 A maximum likelihood fit to data is performed simultaneously in the regions described in section
 406 5. The parameters μ_{WZ+b} , $\mu_{WZ+charm}$, $\mu_{WZ+light}$, where $\mu = \sigma_{\text{observed}}/\sigma_{\text{SM}}$, are extracted
 407 from the fit.

408 8.1 1-jet Fit Results

409 **The results of the fit are currently blinded.** The post-fit yields in each region are summarized
 410 in figure 28.

411 A post-fit summary plot of the 1-jet fitted regions is shown in figure 29:

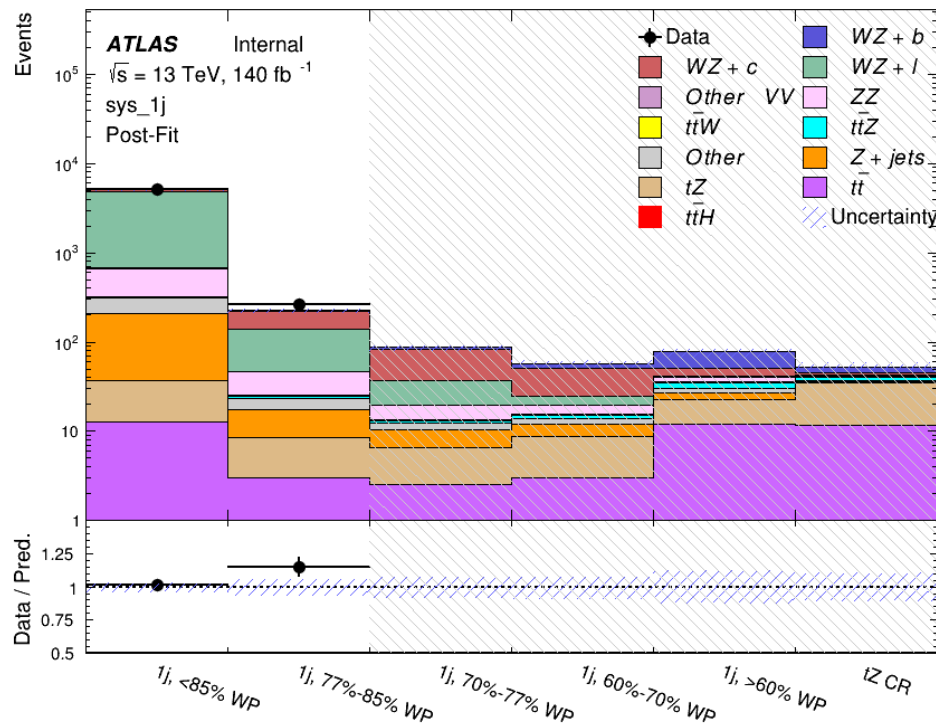


Figure 29: Post-fit summary of the 1-jet fit regions.

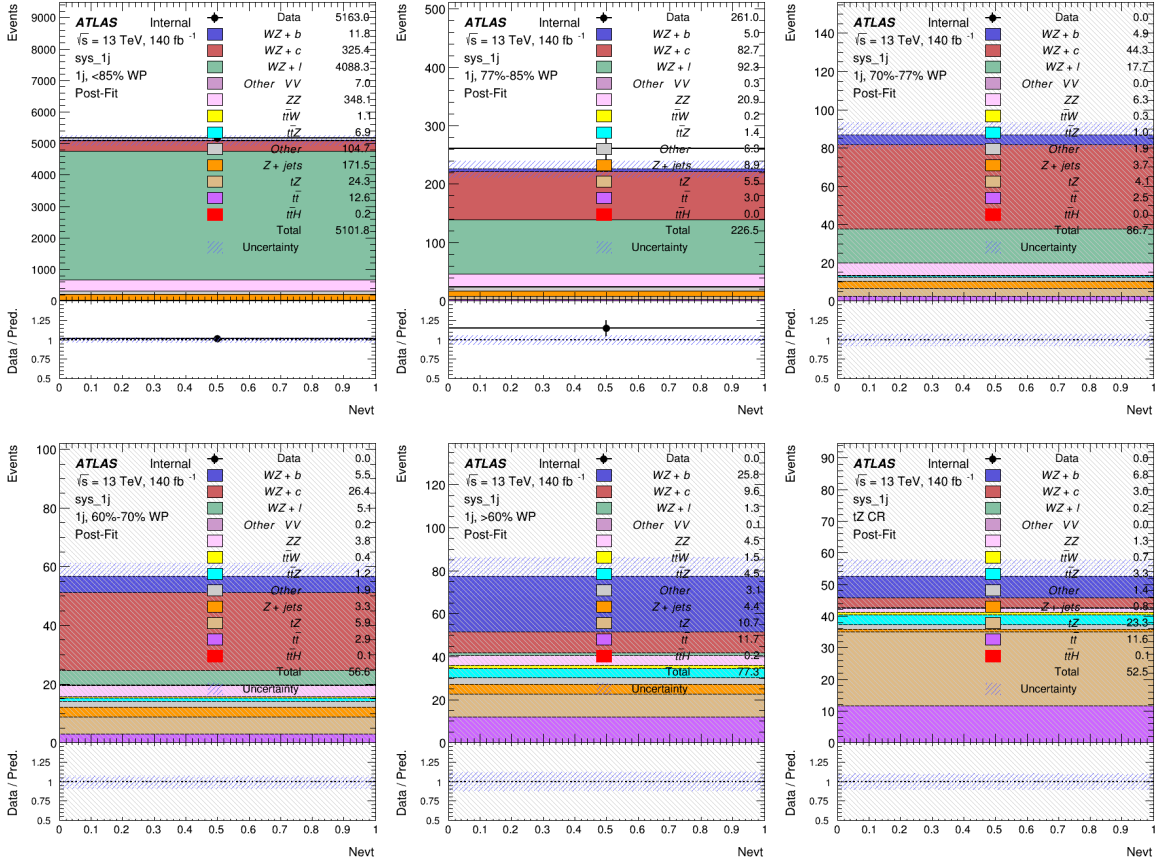


Figure 28: Data/MC results in each of the 1-jet regions after the fit has been performed.

As described in section 7, there are 226 systematic uncertainties that are considered as NPs in the fit. These NPs are constrained by Gaussian or log-normal probability density functions. The latter are used for normalisation factors to ensure that they are always positive. The expected numbers of signal and background events are functions of the likelihood. The prior for each NP is added as a penalty term, decreasing the likelihood as it is shifted away from its nominal value.

The impact of each NP is calculated by performing the fit with the parameter of interest held fixed, varied from its fitted value by its uncertainty, and calculating $\Delta\mu$ relative to the baseline fit. The impact of the most significant sources of systematic uncertainties is summarized in table 14.

Uncertainty Source	$\Delta\mu$	
WZ + charm cross-section	-0.1966	0.2171
tZ cross-section	-0.1521	0.1518
WZ + light cross-section	0.1485	-0.1411
Other VV + b cross-section	-0.1115	0.1163
Flavor Tagging	0.0955	0.0957
Jet Energy Scale	0.0613	0.081
t <bar>t</bar>	-0.0662	0.0654
Luminosity	-0.0609	0.0655
Z + jets cross-section	-0.0284	0.0284
Other VV + charm cross-section	0.0207	-0.0202
Muon Trigger Scale Factor	0.019	0.0209
Total Systematic Uncertainty	0.3511	0.3679

Table 14: Summary of the most significant sources of systematic uncertainty on the measurement of WZ + b with exactly one associated jet.

⁴²² The ranking and impact of those nuisance parameters with the largest contribution to the overall
⁴²³ uncertainty is shown in figure 30.

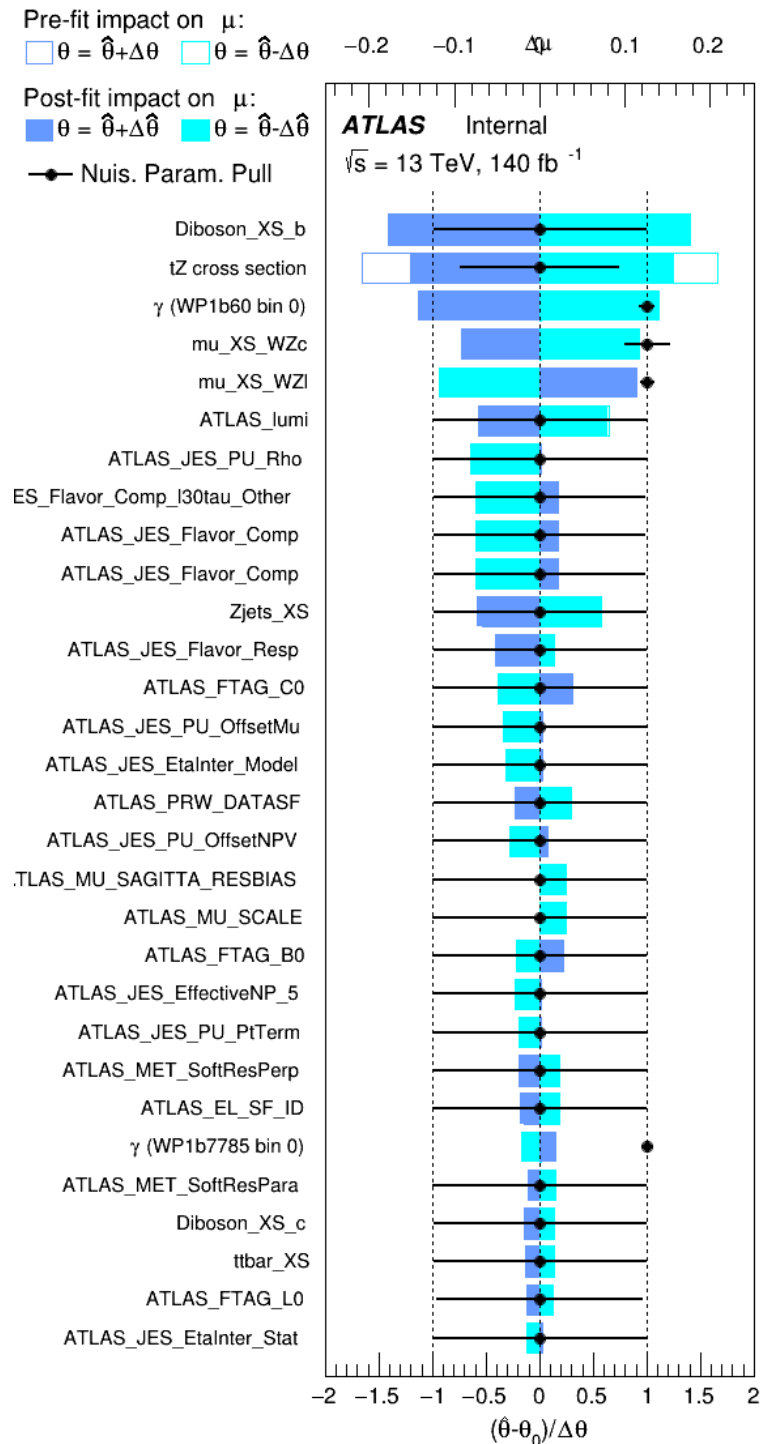


Figure 30: Impact of systematic uncertainties on the signal-strength of $WZ + b$ for events with exactly one jet

424 The large impact of the Jet Energy Scale and Jet Flavor Tagging is unsurprising, as the shape
 425 of the fit regions depends heavily on the modeling of the jets. The other major sources of
 426 uncertainty come from background modelling and cross-section uncertainty. The pie charts in
 427 figure 31 show that for the modelling uncertainties that contribute most correspond to the most
 428 significant backgrounds.

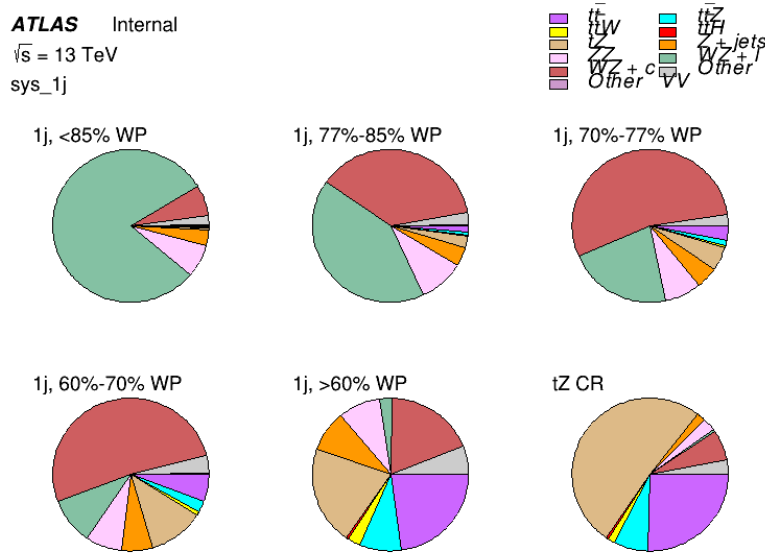


Figure 31: Post-fit background composition of the fit regions.

429 The correlations between these nuisance parameters are summarized in figure 32.

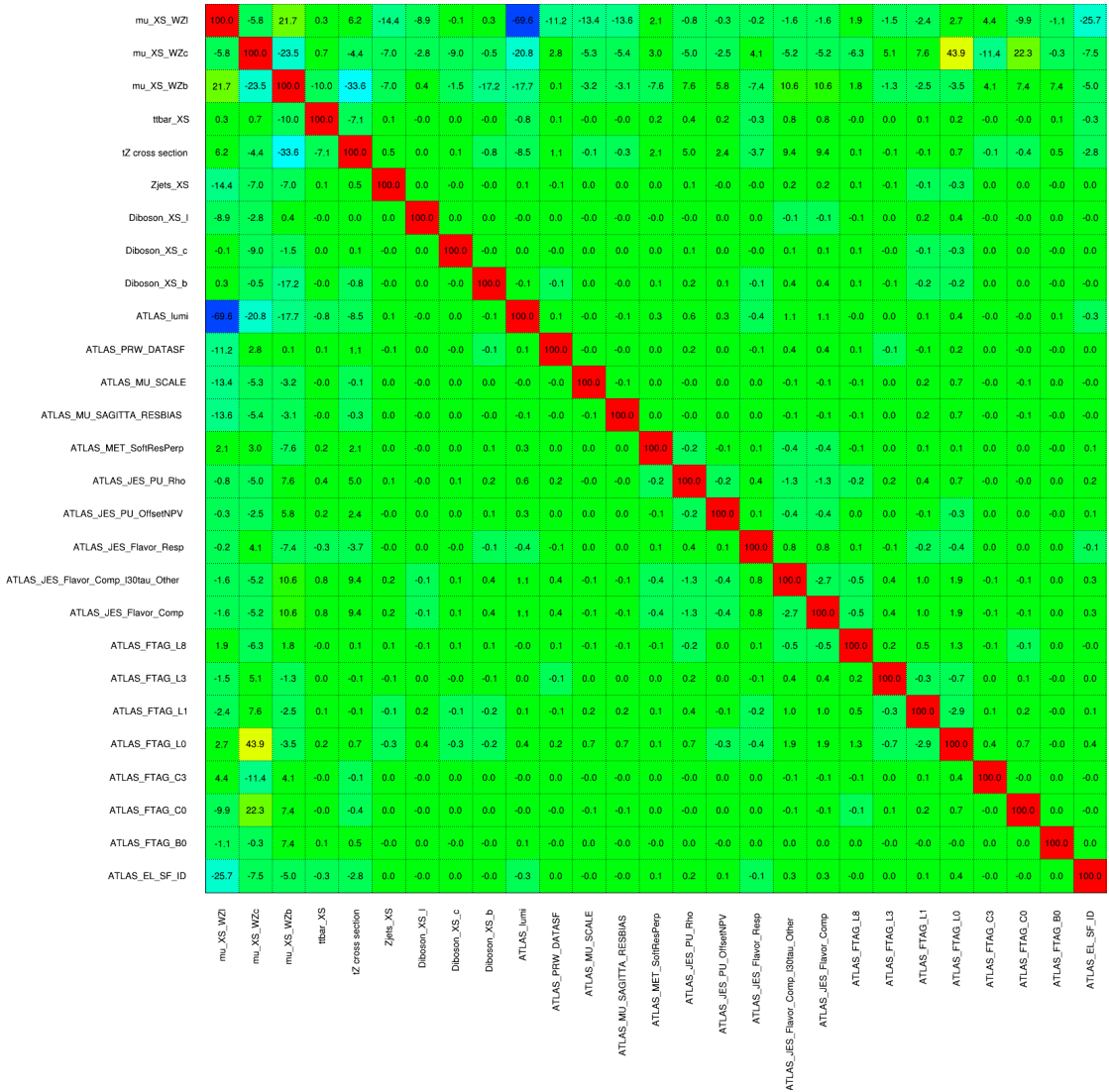


Figure 32: Correlations between nuisance parameters

430 The negative correlations between $\mu_{WZ+charm}$ and μ_{WZ+b} and $\mu_{WZ+light}$ are expected: WZ +
431 charm is present in both the WZ + b and WZ + light enriched regions, therefore increasing the
432 fraction of charm requires increasing the fraction of WZ + b and WZ + light. This reasoning
433 also explains the positive correlation between μ_{WZ+b} and $\mu_{WZ+light}$.

434 Two of the major backgrounds in the region with the highest purity of WZ + b are tZ and Other
435 VV + b, explaining the negative correlations between μ_{WZ+b} and the tZ cross section, and the
436 VV + b cross section.

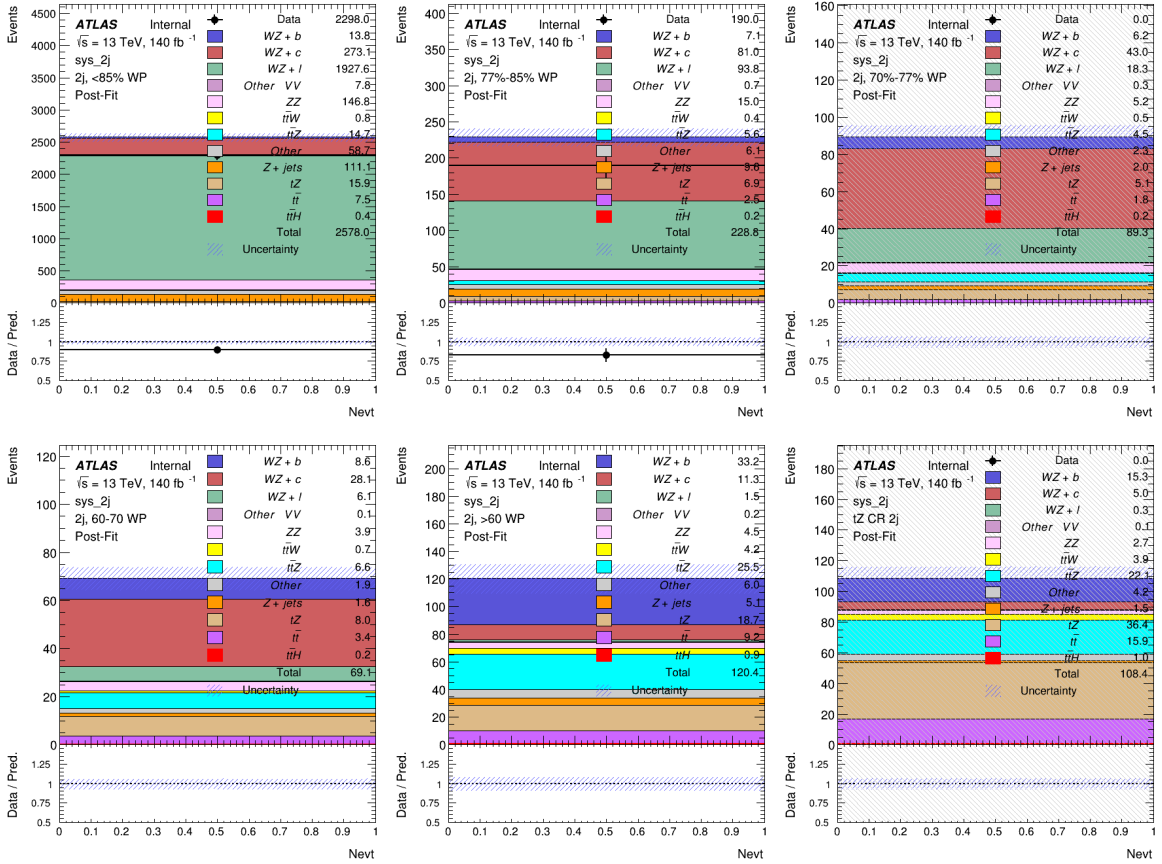


Figure 33: Data/MC results in each of the regions in the 2-jet fit after the fit has been performed.

437 The high correlation between the luminosity and $\mu_{WZ+\text{light}}$ arises from the fact that the uncer-
 438 tainty on $\mu_{WZ+\text{light}}$ is very low (around 4%). Small changes in luminosity cause a change in
 439 the yield of $WZ + \text{light}$ that is large compared to its uncertainty, producing a large correlation
 440 between these two parameters.

441 8.2 2-jet Fit Results

442 **The results of the fit are currently blinded.** The post-fit yields in each region are summarized
 443 in figure 33.

444 A post-fit summary plot of the fitted regions is shown in figure 34:

445 The same set of systematic uncertainties consider for the 1-jet fit are included in the 2-jet fit as
 446 well. The impact of the most significant systematic uncertainties is summarized in table 15.

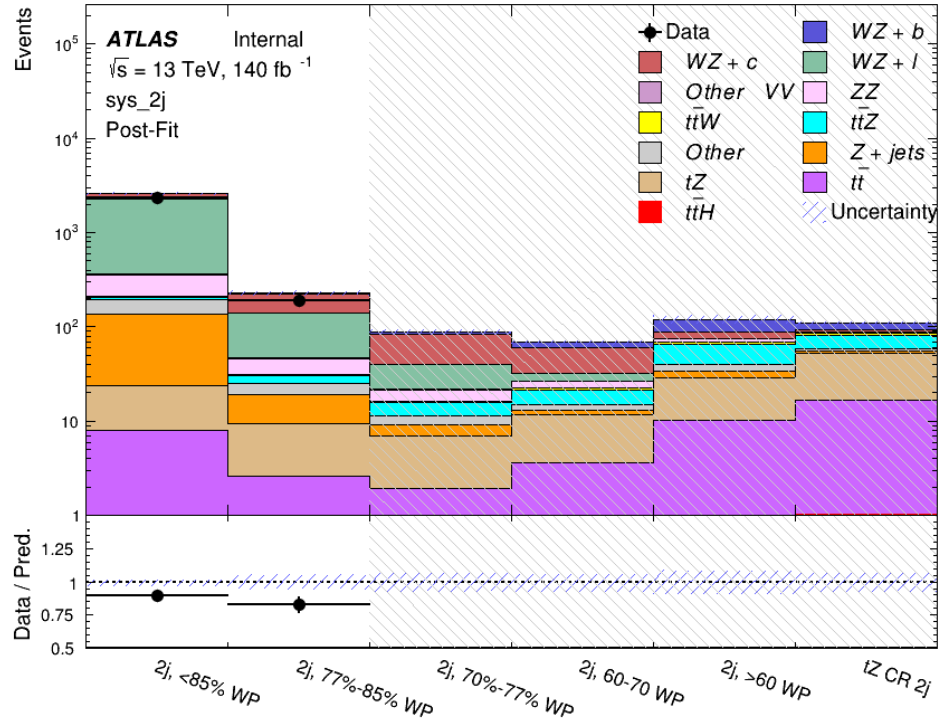


Figure 34: Post-fit summary of the fit over 2-jet regions.

Uncertainty Source	$\Delta\mu$	
WZ + charm cross-section	-0.1966	0.2171
tZ cross-section	-0.1521	0.1518
WZ + light cross-section	0.1485	-0.1411
Other VV + b cross-section	-0.1115	0.1163
Flavor Tagging	0.0955	0.0957
Jet Energy Scale	0.0613	0.081
t <bar>t</bar>	-0.0662	0.0654
Luminosity	-0.0609	0.0655
Z + jets cross-section	-0.0284	0.0284
Other VV + charm cross-section	0.0207	-0.0202
Muon Trigger Scale Factor	0.019	0.0209
Total Systematic Uncertainty	0.3511	0.3679

Table 15: Summary of the most significant sources of systematic uncertainty on the measurement of WZ + b 2-jet events.

The ranking and impact of those nuisance parameters with the largest contribution to the overall uncertainty is shown in figure 35.

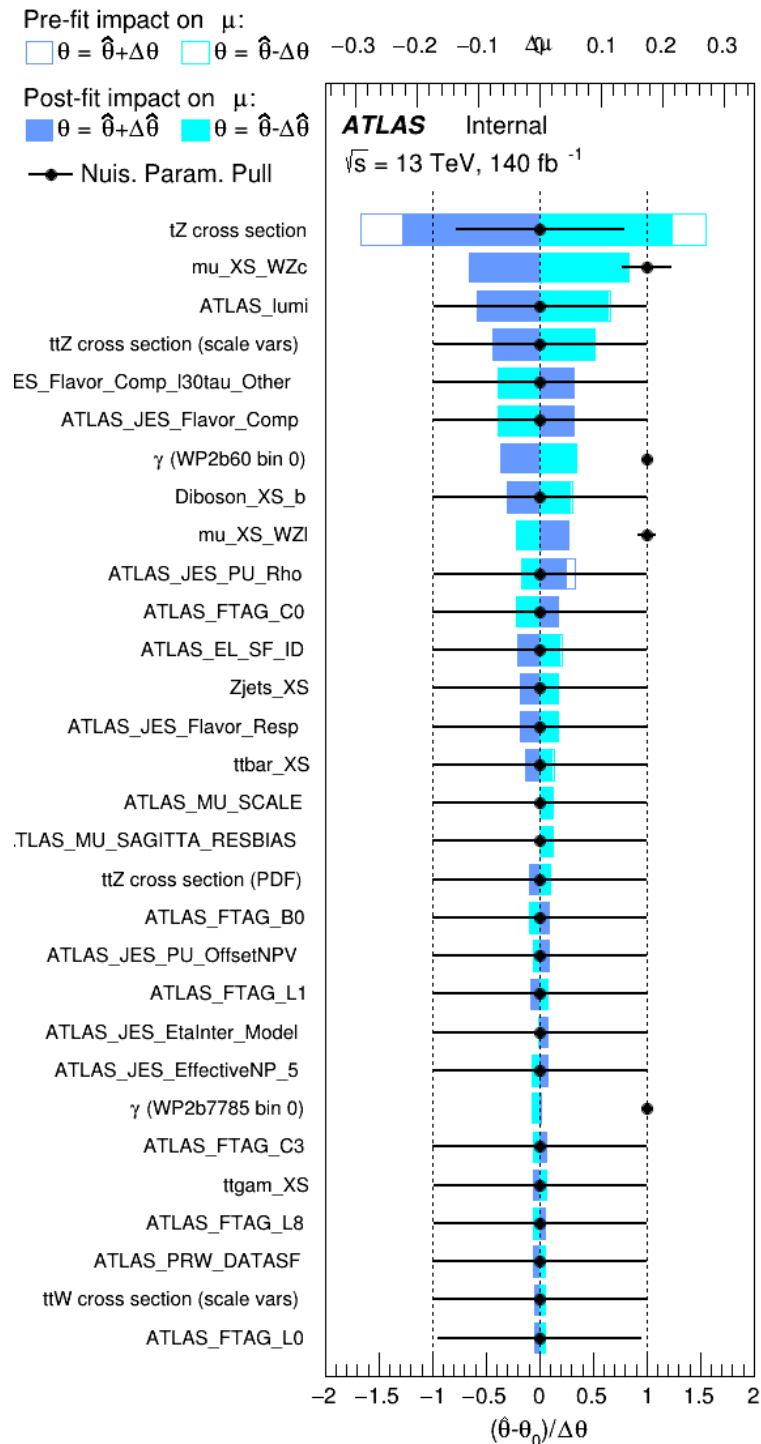


Figure 35: Impact of systematic uncertainties on the signal-strength of $WZ + b$ in 2-jet events.

449 The large impact of the Jet Energy Scale and Jet Flavor Tagging is unsurprising, as the shape
450 of the fit regions depends heavily on the modeling of the jets. The other major sources of
451 uncertainty come from background modelling and cross-section uncertainty. The pie charts in
452 figure 36 show that for the modelling uncertainties that contribute most correspond to the most
453 significant backgrounds.

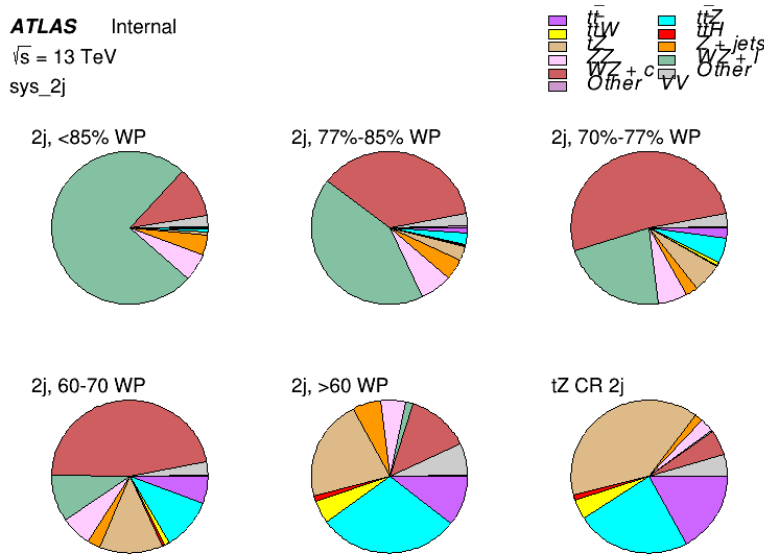


Figure 36: Post-fit background composition of the 2-jet fit regions.

⁴⁵⁴ The correlations between these nuisance parameters are summarized in figure 37.

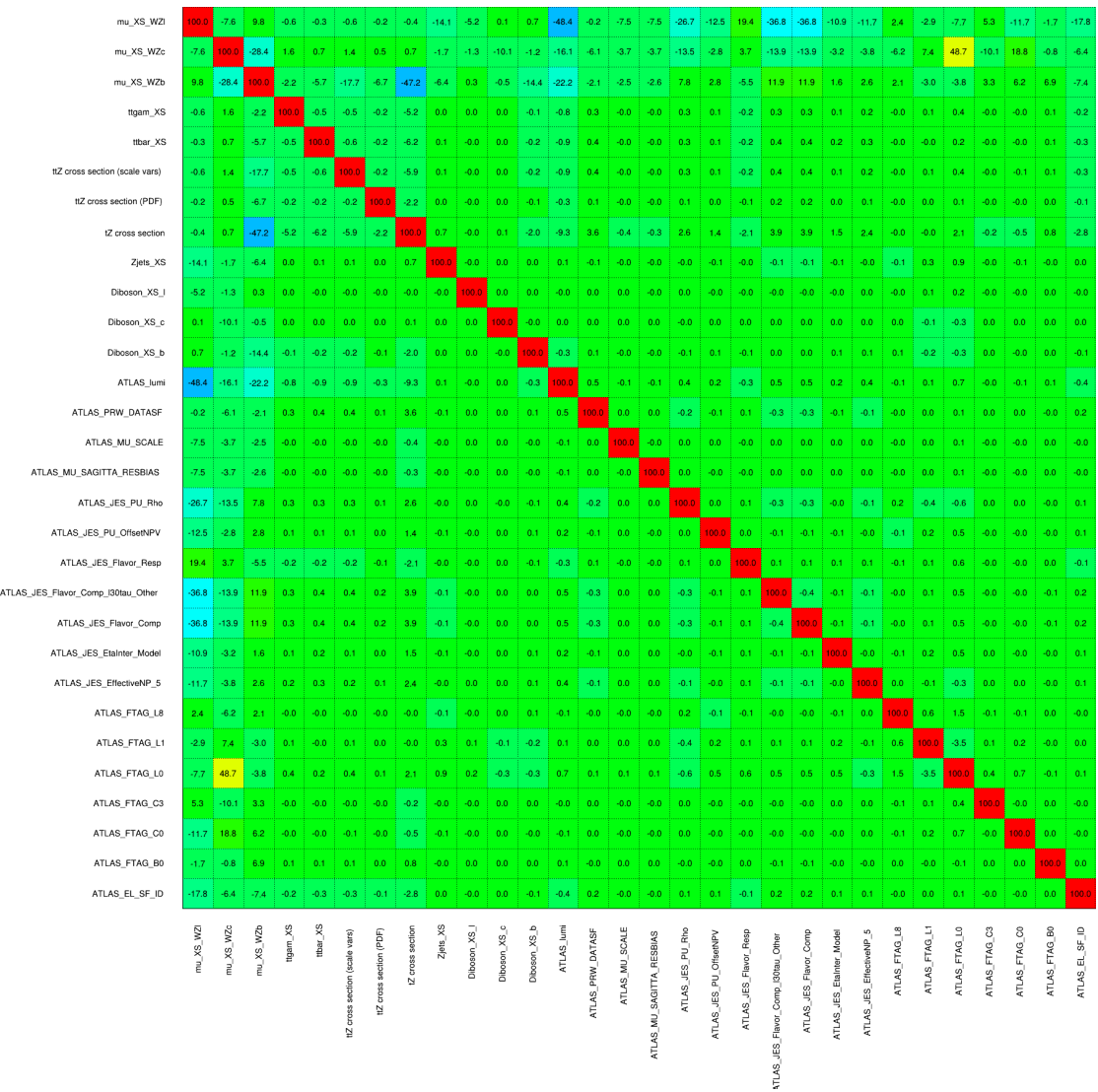


Figure 37: Correlations between nuisance parameters in the 2-jet fit

455 As in the 1-jet case, no significant, unexpected correlations are found between nuisance
456 parameters.

9 Conclusion

458 A measurement of $WZ + \text{heavy flavor}$ is performed using 140 fb^{-1} of $\sqrt{s} = 13 \text{ TeV}$ proton-
459 proton collision data collected by the ATLAS detector at the LHC. This section will be include

460 final results once unblinded.

461 **References**

- 462 [1] M. Aaboud et al. ‘Observation of electroweak $W^\pm Z$ boson pair production in association
463 with two jets in pp collisions at $\sqrt{s} = 13$ TeV with the ATLAS detector’. In: *Phys.
464 Lett.* B793 (2019), pp. 469–492. doi: [10.1016/j.physletb.2019.05.012](https://doi.org/10.1016/j.physletb.2019.05.012). arXiv:
465 [1812.09740 \[hep-ex\]](https://arxiv.org/abs/1812.09740).
- 466 [2] T. Gleisberg et al. ‘Event generation with SHERPA 1.1’. In: *JHEP* 02 (2009), p. 007. doi:
467 [10.1088/1126-6708/2009/02/007](https://doi.org/10.1088/1126-6708/2009/02/007). arXiv: [0811.4622 \[hep-ph\]](https://arxiv.org/abs/0811.4622).
- 468 [3] ATLAS Collaboration. *Electron efficiency measurements with the ATLAS detector using
469 the 2015 LHC proton–proton collision data*. ATLAS-CONF-2016-024. 2016. URL: <https://cds.cern.ch/record/2157687>.
- 470 [4] ATLAS Collaboration. ‘Measurement of the muon reconstruction performance of the
471 ATLAS detector using 2011 and 2012 LHC proton–proton collision data’. In: *Eur. Phys.
472 J. C* 74 (2014), p. 3130. doi: [10.1140/epjc/s10052-014-3130-x](https://doi.org/10.1140/epjc/s10052-014-3130-x). arXiv: [1407.3935
473 \[hep-ex\]](https://arxiv.org/abs/1407.3935).
- 474 [5] *Evidence for the associated production of the Higgs boson and a top quark pair with the
475 ATLAS detector*. Tech. rep. ATLAS-CONF-2017-077. Geneva: CERN, Nov. 2017. URL:
476 <https://cds.cern.ch/record/2291405>.
- 477 [6] ATLAS Collaboration. *Jet Calibration and Systematic Uncertainties for Jets Reconstructed
478 in the ATLAS Detector at $\sqrt{s} = 13$ TeV*. ATL-PHYS-PUB-2015-015. 2015. URL:
479 <https://cds.cern.ch/record/2037613>.
- 480 [7] ATLAS Collaboration. *Selection of jets produced in 13 TeV proton–proton collisions with
481 the ATLAS detector*. ATLAS-CONF-2015-029. 2015. URL: [https://cds.cern.ch/
482 record/2037702](https://cds.cern.ch/record/2037702).
- 483 [8] ATLAS Collaboration. ‘Performance of pile-up mitigation techniques for jets in pp col-
484 lisions at $\sqrt{s} = 8$ TeV using the ATLAS detector’. In: *Eur. Phys. J. C* 76 (2016), p. 581.
485 doi: [10.1140/epjc/s10052-016-4395-z](https://doi.org/10.1140/epjc/s10052-016-4395-z). arXiv: [1510.03823 \[hep-ex\]](https://arxiv.org/abs/1510.03823).
- 486 [9] ATLAS Collaboration. *Performance of missing transverse momentum reconstruction with
487 the ATLAS detector in the first proton–proton collisions at $\sqrt{s} = 13$ TeV*. ATL-PHYS-
488 PUB-2015-027. 2015. URL: <https://cds.cern.ch/record/2037904>.
- 489 [10] P. S. A. Hoecker. ‘TMVA 4 Toolkit for Multivariate Data Analysis with ROOT’. In:
490 *arXiv:physics/0703039* (2013).
- 491 [11] F. Cardillo et al. ‘Measurement of the fiducial and differential cross-section of a top quark
492 pair in association with a Z boson at 13 TeV with the ATLAS detector’. In: ATL-COM-
493 PHYS-2019-334 (Apr. 2019). URL: <https://cds.cern.ch/record/2672207>.

- 495 [12] ATLAS Collaboration. ‘Luminosity determination in pp collisions at $\sqrt{s} = 7$ TeV using
496 the ATLAS detector at the LHC’. In: *Eur. Phys. J. C* 71 (2011), p. 1630. doi: [10.1140/epjc/s10052-011-1630-5](https://doi.org/10.1140/epjc/s10052-011-1630-5). arXiv: [1101.2185 \[hep-ex\]](https://arxiv.org/abs/1101.2185).
- 498 [13] G. Aad et al. ‘Jet energy resolution in proton-proton collisions at $\sqrt{s} = 7$ TeV recorded
499 in 2010 with the ATLAS detector’. In: *The European Physical Journal C* 73.3 (Mar.
500 2013), p. 2306. issn: 1434-6052. doi: [10.1140/epjc/s10052-013-2306-0](https://doi.org/10.1140/epjc/s10052-013-2306-0). URL:
501 <https://doi.org/10.1140/epjc/s10052-013-2306-0>.
- 502 [14] A. Collaboration. ‘Performance of b -jet identification in the ATLAS experiment’. In:
503 *Journal of Instrumentation* 11.04 (2016), P04008. URL: <http://stacks.iop.org/1748-0221/11/i=04/a=P04008>.